

5

Orographically forced flows

Many well-known weather phenomena are directly related to flow over orography, such as mountain waves, lee waves and clouds, rotors and rotor clouds, severe down-slope windstorms, lee vortices, lee cyclogenesis, frontal distortion across mountains, cold-air damming, track deflection of midlatitude and tropical cyclones, coastally trapped disturbances, orographically induced rain and flash flooding, and orographically influenced storm tracks. A majority of these phenomena are mesoscale and are induced by stably stratified flow over orography. Thus, understanding the dynamics associated with stably stratified flow over a mesoscale mountain is essential in improving the prediction of the above mentioned phenomena. In addition, understanding the dynamics of orographically forced flow will also help on different aspects of meteorology, such as turbulence which affects aviation safety, wind-damage risk assessment, pollution dispersion in complex terrain, and subgrid-scale parameterization of mountain wave drag in general circulation models.

5.1 Flows over two-dimensional sinusoidal mountains

Some fundamental properties of flow responses to orographic forcing can be understood by considering a two-dimensional, steady-state, adiabatic, inviscid, nonrotating, Boussinesq fluid flow over a small-amplitude mountain. The governing linear equations can be simplified from (2.2.14)–(2.2.18) to be

$$U \frac{\partial u'}{\partial x} + U_z w' + \frac{1}{\rho_0} \frac{\partial p'}{\partial x} = 0, \quad (5.1.1)$$

$$U \frac{\partial w'}{\partial x} - g \frac{\theta'}{\theta_0} + \frac{1}{\rho_0} \frac{\partial p'}{\partial z} = 0, \quad (5.1.2)$$

$$\frac{\partial u'}{\partial x} + \frac{\partial w'}{\partial z} = 0, \quad (5.1.3)$$

$$U \frac{\partial \theta'}{\partial x} + \frac{N^2 \theta_o}{g} w' = 0. \quad (5.1.4)$$

The above set of equations can be further reduced to *Scorer's equation* (1954),

$$\nabla^2 w' + l^2(z) w' = 0, \quad (5.1.5)$$

where $\nabla^2 = \partial^2/\partial x^2 + \partial^2/\partial z^2$ is the two-dimensional Laplacian operator, and l is the Boussinesq form of the *Scorer parameter* (Scorer 1949), which is defined as:

$$l^2(z) = \frac{N^2}{U^2} - \frac{U_{zz}}{U}. \quad (5.1.6)$$

Equation (5.1.5) serves as a central tool for numerous theoretical studies of small-amplitude, two-dimensional mountain waves, which may also be interpreted as a vorticity equation upon being multiplied by U (Smith 1979). The first term, $U(w'_{xx} + w'_{zz})$, is the rate of change of vorticity following a fluid particle. The second term, $N^2 w'/U$, is the rate of vorticity production by buoyancy forces. The last term, $-U_{zz} w'$, represents the rate of vorticity production by the redistribution of the background vorticity (U_z). In the extreme case of very small Scorer parameter, (5.1.5) reduces to irrotational or potential flow,

$$\nabla^2 w' = 0. \quad (5.1.7)$$

As discussed in Chapter 3 [(3.5.22)], the buoyancy force is negligible in this extreme case. If the forcing is symmetric in the basic flow direction, such as a cylinder in an unbounded fluid or a bell-shaped mountain in a half-plane, then the flow is symmetric. For this particular case, there is no drag produced on the mountain since the fluid is inviscid.

In order to simplify the mathematics of the steady-state mountain wave problem, one may assume that $U(z)$ and $N(z)$ are independent of height, and a sinusoidal terrain

$$h(x) = h_m \sin kx, \quad (5.1.8)$$

where h_m is the mountain height and k is the wave number of the terrain. For an inviscid fluid flow, the lower boundary condition requires the fluid particles to follow the terrain, so that the streamline slope equals the terrain slope locally,

$$\frac{w}{u} = \frac{w'}{U + u'} = \frac{dh}{dx} \quad \text{at} \quad z = h(x). \quad (5.1.9)$$

For a small-amplitude mountain, this leads to the linear lower boundary condition

$$w' = U \frac{dh}{dx} \quad \text{at} \quad z = 0, \quad (5.1.10)$$

or

$$w'(x, 0) = Uh_m k \cos kx \quad \text{at} \quad z = 0, \quad (5.1.11)$$

for flow over a sinusoidal mountain as described by (5.1.8). Due to the sinusoidal nature of the forcing, it is natural to look for solutions in terms of sinusoidal functions,

$$w'(x, z) = w_1(z) \cos kx + w_2(z) \sin kx. \quad (5.1.12)$$

Substituting the above solution into (5.1.5) with a constant Scorer parameter leads to

$$w_{izz} + (\ell^2 - k^2)w_i = 0, \quad i = 1, 2. \quad (5.1.13)$$

As discussed in Chapter 3 [(3.5.7)], two cases are possible: (a) $\ell^2 < k^2$ and (b) $\ell^2 > k^2$. The first case requires $N/U < k$ or $Na/U < 2\pi$, where a is the terrain wavelength. Physically, this means that the basic flow has relatively weaker stability and stronger wind, or that the mountain is narrower than a certain threshold. For example, to satisfy the criterion for a flow with $U = 10 \text{ m s}^{-1}$ and $N = 0.01 \text{ s}^{-1}$, the wavelength of the mountain should be smaller than 6.3 km. In fact, this criterion can be rewritten as $(a/U)/(2\pi/N) < 1$. The numerator, a/U , represents the advection time of an air parcel passing over one wavelength of the terrain, while the denominator, $2\pi/N$, represents the period of buoyancy oscillation due to stratification. This means that the time an air parcel takes to pass over the terrain is less than it takes for vertical oscillation due to buoyancy force. In other words, buoyancy force plays a smaller role than the horizontal advection. In this situation, (5.1.13) can be rewritten as

$$w_{izz} - (k^2 - \ell^2)w_i = 0, \quad i = 1, 2. \quad (5.1.14)$$

The solutions of the above second-order differential equation with constant coefficient may be obtained

$$w_i = A_i e^{\lambda z} + B_i e^{-\lambda z}, \quad i = 1, 2, \quad (5.1.15)$$

where

$$\lambda = \sqrt{k^2 - \ell^2}. \quad (5.1.16)$$

Similar to that described in Section 3.4, the upper boundedness condition requires $A_i = 0$ because the energy source is located at $z = 0$. Applying the lower boundary condition, (5.1.11), and the upper boundary condition ($A_i = 0$) to (5.1.15) yields

$$B_1 = Uh_m k; \quad B_2 = 0. \quad (5.1.17)$$

This gives the solution,

$$w'(x, z) = w_1(z) \cos kx = Uh_m k e^{-\sqrt{k^2 - \ell^2} z} \cos kx, \quad (5.1.18)$$

The vertical displacement (η) is defined as $w' = D\eta/Dt$ which reduces to

$$w' = \frac{D\eta}{Dt} = U \frac{\partial \eta}{\partial x} \quad (5.1.19)$$

for a steady-state flow.

Equation (5.1.18) can then be expressed in terms of η ,

$$\eta = \frac{1}{U} \int_0^x w' dx = h_m \sin kx e^{-\sqrt{k^2 - \bar{P}^2} z}. \quad (5.1.20)$$

The above solution is sketched in Fig. 5.1a. The disturbance is symmetric with respect to the vertical axis and decays exponentially with height. Thus, the flow belongs to the evanescent flow regime as discussed in Section 3.5. The buoyancy force plays a minor role compared to that of the advection effect. The other variables can also be obtained by using the governing equations and (5.1.18),

$$u' = U h_m \sqrt{k^2 - \bar{P}^2} \sin kx e^{-\sqrt{k^2 - \bar{P}^2} z}, \quad (5.1.21)$$

$$p' = -\rho_0 U^2 h_m \sqrt{k^2 - \bar{P}^2} \sin kx e^{-\sqrt{k^2 - \bar{P}^2} z}, \quad (5.1.22)$$

$$\theta' = -(\theta_0 N^2 / g) h_m \sin kx e^{-\sqrt{k^2 - \bar{P}^2} z}. \quad (5.1.23)$$

The maxima and minima of u' , p' , and θ' are also denoted in Fig. 5.1a. The coldest (warmest) air is produced at the mountain peak (valley) due to adiabatic cooling (warming). The flow accelerates over the mountain peaks and decelerates over the

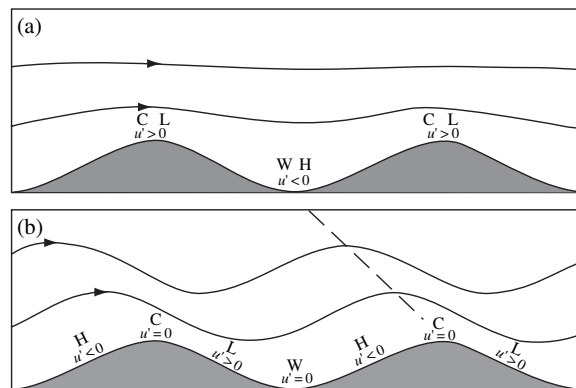


Fig. 5.1 The steady-state, inviscid flow over a two-dimensional sinusoidal mountain when (a) $\bar{l}^2 < k^2$ (or $N < kU$), where k is the terrain wavenumber ($= 2\pi/a$, where a is the terrain wave length), or (b) $\bar{l}^2 > k^2$ (or $N > kU$). The dashed line in (b) denotes the upstream tilt of the constant phase line. The maxima and minima of u' , p' (H and L), and θ' (W and C) are denoted in the figures.

valleys. From the horizontal momentum equation, (5.1.1) with $U_z = 0$, or (5.1.22), a low (high) pressure is produced over the mountain peak (valley) where maximum (minimum) wind is produced. Note that (5.1.1) is also equivalent to the *Bernoulli equation*, which states that the pressure perturbation is out of phase with the horizontal velocity perturbation. Since no pressure difference exists between the upslope and downslope, this flow produces no net wave drag on the mountain (mountain drag). The *mountain drag* can be computed either from the horizontal pressure force on the mountain over a wavelength,

$$\mathcal{D} = \frac{k}{2\pi} \int_{-\pi/k}^{\pi/k} p'(x, z = 0) \left(\frac{dh}{dx} \right) dx, \quad (5.1.24)$$

or equivalently, as the negative of the vertical flux of horizontal momentum (*momentum flux*) in the wave motion,

$$\mathcal{D} = -\frac{\rho_0 k}{2\pi} \int_{-\pi/k}^{\pi/k} u' w' dx. \quad (5.1.25)$$

Note that *Eliassen and Palm's theorem*, (4.4.10), indicates that the vertical flux of horizontal momentum in a steady-state flow is negatively proportional to the vertical energy flux, $\overline{p'w'}$ (where the overbar denotes the average over a wavelength).

In the second case, $l^2 > k^2$, the flow response is completely different. This case requires $N/U > k$ or $Na/U > 2\pi$. As discussed in Section 3.5, this means that the basic flow has relatively stronger stability and weaker wind or that the mountain is wider. For example, and as mentioned earlier, to satisfy the criterion for a flow with $U = 10 \text{ m s}^{-1}$ and $N = 0.01 \text{ s}^{-1}$, the terrain wavelength should be larger than 6.3 km. Since $(a/U)/(2\pi/N) > 1$, the advection time is larger than the period of the vertical oscillation. In other words, buoyancy force plays a more dominant role than the horizontal advection. In this case, (5.1.13) can be written as

$$w_{izz} + m^2 w_i = 0, \quad m^2 = l^2 - k^2, \quad i = 1, 2. \quad (5.1.26)$$

We look for solutions in the form

$$w_i(z) = A_i \sin mz + B_i \cos mz, \quad i = 1, 2. \quad (5.1.27)$$

Substituting (5.1.27) into (5.1.12) leads to

$$w'(x, z) = C \cos(kx + mz) + D \sin(kx + mz) + E \cos(kx - mz) + F \sin(kx - mz). \quad (5.1.28)$$

In the above equation, terms of $(kx + mz)$ have an upstream phase tilt with height, while terms of $(kx - mz)$ have a downstream phase tilt. It can be shown that terms of $(kx + mz)$ have a positive vertical energy flux and should be retained since the

energy source in this case is located at the mountain surface. This satisfies the Sommerfeld radiation boundary condition, as discussed in Section 4.4. Thus, the solution requires $E = F = 0$. This flow regime is characterized as the upward propagating wave regime, as discussed in Chapter 3. As in the first case, the lower boundary condition requires

$$C = Uh_m k, \quad D = 0. \quad (5.1.29)$$

This leads to

$$w'(x, z) = Uh_m k \cos(kx + mz). \quad (5.1.30)$$

Other variables can be obtained through definitions or the governing equations,

$$\eta(x, z) = h_m \sin(kx + mz), \quad (5.1.31)$$

$$u'(x, z) = -Uh_m m \cos(kx + mz), \quad (5.1.32)$$

$$p'(x, z) = \rho_o U^2 h_m m \cos(kx + mz), \quad \text{and} \quad (5.1.33)$$

$$\theta'(x, z) = -\frac{N^2 \theta_o h_m}{g} \sin(kx + mz). \quad (5.1.34)$$

The vertical displacement of the flow, and the maxima and minima of u' , p' , and θ' are depicted in Fig. 5.1b. Note that the flow pattern is no longer symmetric. The constant phase lines are tilted upstream (to the left) with height, thus producing a high pressure on the windward slope and a low pressure on the lee slope. Based on (5.1.32) or the Bernoulli equation (5.1.1), the flow decelerates over the windward slope and accelerates over the lee slope. The coldest and warmest spots are still located over the mountain peaks and valleys, respectively. The mountain drag can be calculated either from (5.1.24) or (5.1.25) to be

$$\mathcal{D} = \frac{1}{2} \rho_o U^2 h_m^2 k \sqrt{l^2 - k^2}. \quad (5.1.35)$$

The positive wave drag on the mountain is produced by the high pressure on the windward slope and the low pressure on the lee slope. This also can be understood through (5.1.25) and the out-of-phase relationship of u' and w' over the windward and lee slopes, as shown in Fig. 5.1b.

When $l^2 \gg k^2$, the flow approaches a limiting case in which the buoyancy effect dominates and the advection effect is totally negligible. In other words, the vertical pressure gradient force and the buoyancy force are roughly in balance and the vertical acceleration can be ignored. Thus, the mountain waves become hydrostatic. In this limiting case, the governing equation becomes

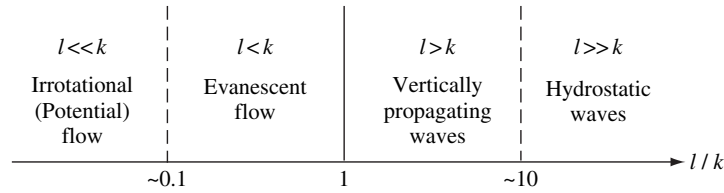


Fig. 5.2 Relations among different mountain wave regimes as determined by l/k , where l is the Scorer parameter and k is the wave number.

$$w'_{zz} + l^2 w' = 0. \tag{5.1.36}$$

The flow pattern repeats itself in the vertical with a wavelength of $\lambda_z = 2\pi/l = 2\pi U/N$, which is also referred to as the hydrostatic vertical wavelength. The regime boundary between the regimes of vertically propagating waves and evanescent waves can be found by letting $l=k$, which leads to $a = 2\pi U/N$. The relation among the mountain waves discussed in this subsection is sketched in Fig. 5.2.

5.2 Flows over two-dimensional isolated mountains

5.2.1 Uniform basic flow

The mountain wave problem in Section 5.1 may be extended to be more realistic by assuming an isolated mountain. Taking the one-sided Fourier transform (Appendix 5.1) of (5.1.5) yields

$$\hat{w}_{zz} + (l^2 - k^2)\hat{w} = 0. \tag{5.2.1}$$

The Fourier transform of the linear lower boundary condition, (5.1.10), is

$$\hat{w}(k, z = 0) = ikU \hat{h}(k). \tag{5.2.2}$$

For constant Scorer parameter, the solution of (5.2.1) can be written into two parts,

$$\hat{w}(k, z) = \hat{w}(k, 0)e^{i\sqrt{l^2 - k^2}z} \quad \text{for } l^2 > k^2 \text{ and} \tag{5.2.3a}$$

$$\hat{w}(k, z) = \hat{w}(k, 0)e^{-\sqrt{k^2 - l^2}z} \quad \text{for } l^2 < k^2. \tag{5.2.3b}$$

Taking the inverse one-sided Fourier transform of (5.2.3) yields the solution in the physical space,

$$w'(x, z) = 2\text{Re} \left[\int_0^l ikU \hat{h}(k)e^{i\sqrt{l^2 - k^2}z} e^{ikx} dk + \int_l^\infty ikU \hat{h}(k)e^{-\sqrt{k^2 - l^2}z} e^{ikx} dk \right], \tag{5.2.4}$$

where Re represents the real part. The first integration on the right-hand side of (5.2.4) represents the upward propagating wave which satisfies the upper radiation boundary

condition, while the second integration represents the evanescent wave which satisfies the boundedness upper boundary condition. Note that (5.2.4) is for a continuous spectrum of Fourier modes, instead of just one single mode as considered in Section 5.1.

For simplicity, let us consider a bell-shaped mountain or the *Witch of Agnesi* mountain profile,

$$h(x) = \frac{h_m a^2}{x^2 + a^2}, \quad (5.2.5)$$

where h_m is the mountain height and a is the half-width where the mountain height is $h_m/2$. The advantage of using a bell-shaped mountain lies in that its one-sided Fourier transform (Appendix 5.1) is in a simple form,

$$\hat{h}(k) = \frac{h_m a}{2} e^{-ka}, \quad \text{for } k > 0. \quad (5.2.6)$$

The Fourier transform for any k is $(h_m a/2) \exp(-|k|a)$. First, we will center our discussion on the extreme case with $l^2 \ll k^2$ (i.e., $al \ll 1$ or $Na \ll U$). Note that for bell-shaped mountains, we assume $k \approx 1/a$, instead of $k = 2\pi/a$ for sinusoidal mountains. As discussed earlier, the flow becomes a potential flow in which the buoyancy plays a negligible role. In this case, (5.2.4) can be approximated by

$$\begin{aligned} w'(x, z) &\approx 2\text{Re} \left[U \int_0^\infty ik \hat{h}(k) e^{-kz} e^{ikx} dk \right] \\ &= 2\text{Re} \left[U \int_0^\infty ik \left(\frac{h_m a}{2} \right) e^{-ka} e^{-kz} e^{ikx} dk \right]. \end{aligned} \quad (5.2.7)$$

Since $w = U\partial\eta/\partial x$, the Fourier transform of η can be obtained from that of \hat{w} ,

$$\hat{\eta}(k, z) = \frac{\hat{w}(k, z)}{ikU}. \quad (5.2.8)$$

Substituting (5.2.7) into (5.2.8) leads to

$$\eta(x, z) = h_m a \text{Re} \int_0^\infty e^{-k(z+a-ix)} dx = \frac{h_m a(z+a)}{x^2 + (z+a)^2}. \quad (5.2.9)$$

Therefore, similar to the sinusoidal mountain case, the flow pattern is symmetric with respect to the center of the mountain ridge ($x = 0$). However, the amplitude decreases with height linearly, instead of exponentially. The flow pattern is depicted in Fig. 5.3a.

Second, let us consider another extreme case: $l^2 \gg k^2$ (i.e., $al \gg 1$ or $Na \gg U$). As discussed in Section 5.1, the vertical acceleration due to the buoyancy force plays a dominant role. In this case, the solution (5.2.4) can be approximated by

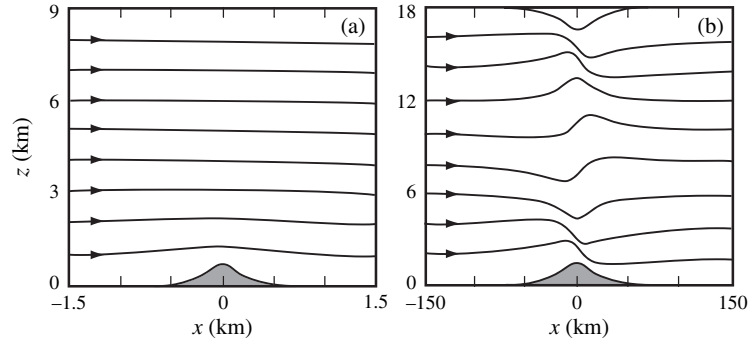


Fig. 5.3 Streamlines of steady-state flow over an isolated, bell-shaped mountain when (a) $l^2 \ll k^2$ (or $Na \ll U$), where a is the half-width of the mountain, or (b) $l^2 \gg k^2$ (or $Na \gg U$). (Adapted after Durran 1990.)

$$w'(x, z) \approx 2\text{Re} \left[U \int_0^\infty ik \hat{h}(k) e^{ilz} e^{ikx} dk \right] = 2\text{Re} \left[U \int_0^\infty ik \left(\frac{h_m a}{2} \right) e^{-ka} e^{ilz} e^{ikx} dk \right]. \quad (5.2.10)$$

Similarly, the vertical displacement can be obtained,

$$\eta(x, z) = 2\text{Re} \int_0^\infty \frac{h_m a}{2} e^{-ka} e^{i(kx+lz)} dk = \frac{h_m a (a \cos lz - x \sin lz)}{x^2 + a^2}. \quad (5.2.11)$$

This type of flow is characterized as a hydrostatic mountain wave. The disturbance confines itself over the mountain in horizontal, but repeats itself in vertical with a wavelength of $2\pi U/N$. Without the Boussinesq approximation, the above solution becomes

$$\eta(x, z) = \left(\frac{\rho_s}{\rho(z)} \right)^{1/2} \left[\frac{h_m a (a \cos lz - x \sin lz)}{x^2 + a^2} \right], \quad (5.2.12)$$

where ρ_s is the air density near surface. Equation (5.2.12) indicates that the wave amplitude will increase with a decreased air density of the basic flow. That is, the wave amplitude will increase at higher altitudes since air density decreases with height in a stably stratified flow. This helps explain the wave amplification in the higher atmosphere, such as large-amplitude gravity waves in the stratosphere. As described in Section 5.1, other fields can be obtained by the governing equations, (5.1.1)–(5.1.4) with $U_z = 0$. The wave drag on the mountain surface in this hydrostatic limit can be obtained by applying the Parseval theorem (Appendix 5.1),

$$\mathcal{D} = \int_{-\infty}^\infty p'(x, z=0) \frac{dh}{dx} dx = \int_{-\infty}^\infty p'(x, 0) \frac{dh^*}{dx} dx = \frac{\pi}{4} \rho_o U N h_m^2 \quad (5.2.13)$$

where h^* is the complex conjugate of h . The momentum is transferred to a level where the wave breaks down, which is not included in the linear theory.

Third, an asymptotic solution can be obtained for the case with $l^2 \approx k^2$ (i.e., $al \approx 1$ or $Na \approx U$). In this case, all terms of the vertical momentum equation, (5.1.2) are equally important. Both asymptotic methods and numerical methods have been applied to solve the problem. In the following, we apply the *stationary phase method* to this particular problem. We look for solutions far downstream, $x \rightarrow \infty$ in (5.2.4). In this limit, the second term on the right side of (5.2.4) approaches 0 due to fast oscillation of $\exp(ikx)$, according to the Riemann–Lebesgue Lemma (Appendix 5.1). For large x , we have

$$\eta(x, z) \approx 2\text{Re} \int_0^l \hat{h}(k) e^{i\phi(k)} dk, \quad (5.2.14)$$

where

$$\phi(k) = \sqrt{l^2 - k^2} z + kx \quad (5.2.15)$$

is a phase function. Based on the stationary phase method, we will look for a particular k^* such that

$$\frac{d\phi}{dk} = 0 \quad \text{at} \quad k = k^*, \quad (5.2.16)$$

where k^* is called the *point of stationary phase*. With large x or z , $\exp(i\phi)$ will oscillate rapidly and, therefore, η will approach 0, according to the Riemann–Lebesgue Lemma. However, near k^* , the contribution to the integration by $\exp(i\phi)$ still remains because ϕ is approximately constant. Substituting the phase function (5.2.15) into (5.2.16) leads to the *influence function*,

$$\frac{z}{x} = \frac{\sqrt{l^2 - k^{*2}}}{k^*}, \quad (5.2.17)$$

in the region near k^* . Taking the Taylor's series expansion of $\phi(k)$ near k^* gives

$$\phi(k) = \phi(k^*) + \left[\frac{\partial \phi}{\partial k} \right]_{k^*} \tilde{k} + \frac{1}{2!} \frac{\partial^2 \phi}{\partial k^2} \tilde{k}^2 + \dots, \quad (5.2.18)$$

where $\tilde{k} = k - k^*$. The second term on the right side of the above equation disappears due to the definition of k^* in (5.2.16). Thus, (5.2.14) becomes

$$\eta(x, z) = 2\text{Re} \left[\hat{h}(k^*) e^{i\phi(k^*)} \int_0^l e^{i\phi_{kk} \tilde{k}^2 / 2} d\tilde{k} \right]. \quad (5.2.19)$$

For a bell-shaped mountain,

$$\eta(x, z) = \sqrt{2\pi} h_m a e^{-k^* a} \left[\frac{(l^2 - k^{*2})^{3/4}}{l z^{1/2}} \right] \cos \left(\sqrt{l^2 - k^{*2}} z + k^* x - \frac{\pi}{4} \right), \quad (5.2.20)$$

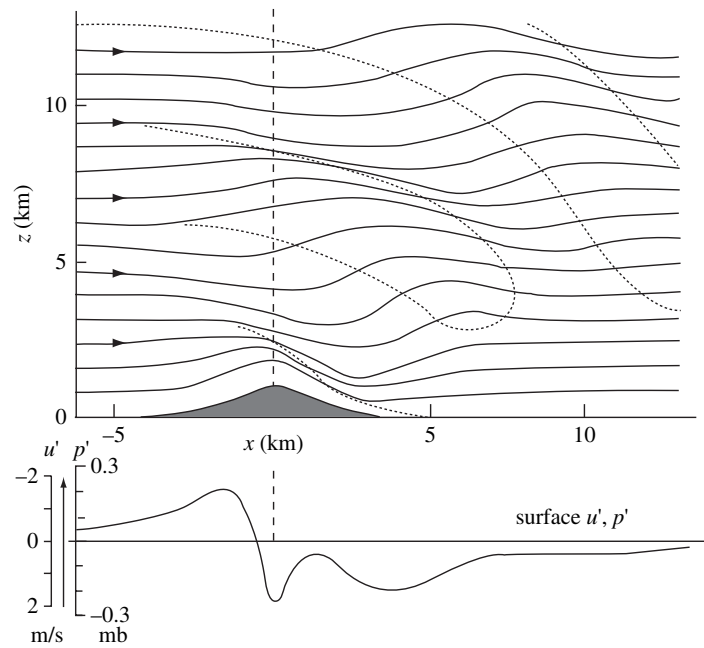


Fig. 5.4 Flow over a two-dimensional ridge of intermediate width ($l^2 \approx k^2$ or $al = Na/U = 1$) where the buoyancy force is important, but not so dominant that the flow is hydrostatic. The waves on the lee aloft are the *dispersive tail* of the nonhydrostatic waves ($k < l$, but not $k \ll l$). (Adapted after Queney 1948.)

where

$$k^* = \frac{l}{\sqrt{(z/x)^2 + 1}}. \quad (5.2.21)$$

Figure 5.4 shows an example of a flow over a ridge of intermediate width ($l^2 \approx k^2$) where the buoyancy force is important, but not so dominant that the flow becomes hydrostatic. The nearly periodic waves located to the upper right of the mountain are the *dispersive tail* of nonhydrostatic waves with k less than, but not much less than l .

In fact, the influence function, (5.2.17), is related to the energy propagation associated with the mountain waves. The group velocity (c_{gm}) in the frame of reference fixed with the mountain can be obtained from (3.5.11),

$$\mathbf{c}_{gm} = \left(U + \frac{\partial \omega}{\partial k} \right) \mathbf{i} + \frac{\partial \omega}{\partial m} \mathbf{k}, \quad (5.2.22)$$

where m stands for mountain and

$$\omega = \frac{-Nk}{\sqrt{k^2 + m^2}}. \quad (5.2.23)$$

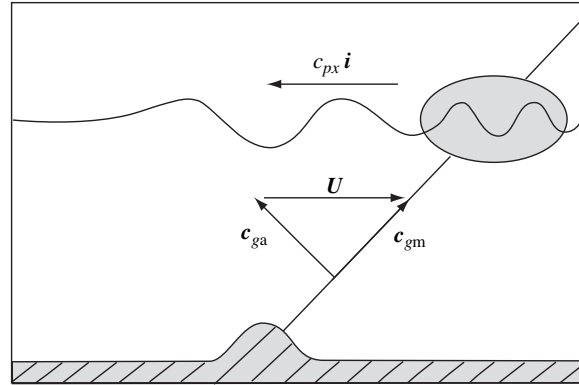


Fig. 5.5 A schematic illustrating the relationship among the group velocity with respect to (w.r.t) the air (c_{ga}), group velocity w.r.t the mountain (c_{gm}), horizontal phase speed ($c_{px}\mathbf{i}$), and the basic wind. The horizontal phase speed of the wave is exactly equal and opposite to the basic wind speed. The wave energy propagates upward and upstream relative to the air, but is advected downstream by the basic wind. The energy associated with the mountain waves propagates upward and downstream relative to the mountain. (After Smith 1979, reproduced with permission from Elsevier.)

Substituting (5.2.23) into (5.2.22) leads to

$$\mathbf{c}_{gm} = U\mathbf{i} + \mathbf{c}_{ga} = \left[U - \frac{Nm^2}{(k^2 + m^2)^{3/2}} \right] \mathbf{i} + \left[\frac{Nkm}{(k^2 + m^2)^{3/2}} \right] \mathbf{k}, \quad (5.2.24)$$

where \mathbf{c}_{ga} is the group velocity relative to the air. Furthermore, the requirement of stationary waves, $c_{px} + U = 0$, implies

$$U = \frac{N}{\sqrt{k^2 + m^2}}. \quad (5.2.25)$$

In (5.2.23), the negative sign is chosen in order to obtain positive c_{gz} by assuming positive k and m due to the use of one-sided Fourier transform. The relationship among $c_{px}\mathbf{i}$, \mathbf{c}_{gm} and \mathbf{c}_{ga} is sketched in Fig. 5.5. The upstream phase speed of the mountain wave is exactly equal to and opposite of the basic wind speed. The wave energy propagates upward and upstream relative to the air, but is advected downstream by the basic wind. Thus, relative to the mountain, the energy associated with the mountain waves propagates upward and downstream. The slope of the group velocity can be obtained by substituting U of (5.2.25) into (5.2.24) and then calculating the slope,

$$\frac{c_{gz}}{c_{gx}} = \frac{m}{k} = \sqrt{\frac{N^2}{U^2 k^2} - 1} = \frac{\sqrt{l^2 - k^2}}{k} = \frac{z}{x}. \quad (5.2.26)$$

In deriving the second equality, we have used (5.2.25), while in deriving the last equality, we have used (5.2.17) near the *point of stationary phase*, i.e. $k = k^*$.

Therefore, the point of stationary phase is the value of k corresponding to a wave with a group velocity beam as shown in Fig. 5.5. Waves are found downstream since the horizontal group velocity is less than the phase speed.

For general cases, such as $l^2 < k^2$ or $l^2 > k^2$, it is not easy to obtain analytical solutions from (5.2.4). With the advancement of numerical techniques, such as the Fast Fourier Transform (FFT), and computers, solutions can be approximately obtained numerically with the implementation of proper boundary conditions.

5.2.2 Basic flow with variable Scorer parameter

In the real atmosphere, the basic wind and stratification normally vary with height. To study the mountain waves produced by this type of basic flow, we assume that the Scorer parameter, (5.1.6), is a slowly varying function of z . In this situation, we expect to find a solution of (5.2.1) in form of,

$$\hat{w}(k, z) = A(k, z)e^{i\phi(k, z)}, \quad (5.2.27)$$

where $A(k, z)$ is a slow-varying amplitude function, and $\phi(k, z)$ is the slow-varying phase function. Substituting (5.2.27) into (5.2.1) yields

$$[-A\phi_z^2 + (l^2 - k^2)A] + i(A\phi_{zz} + 2A_z\phi_z) + A_{zz} = 0. \quad (5.2.28)$$

The last term makes a minor contribution and can be neglected, since $A(k, z)$ is a slow-varying function of z . Thus, the above equation reduces to

$$\phi_z = \sqrt{l^2 - k^2}, \quad \text{and} \quad (5.2.29)$$

$$\frac{\partial}{\partial z}(A^2\phi_z) = 0. \quad (5.2.30)$$

Combining the above two equations leads to

$$A^2\sqrt{l^2 - k^2} = \text{constant}. \quad (5.2.31)$$

For long (hydrostatic) waves ($l^2 \gg k^2$), the above equation reduces to

$$A^2l = \text{constant}. \quad (5.2.32)$$

This implies that the amplitude of the vertical velocity increases (decreases) significantly in regions of weak (strong) stratification or strong (weak) wind. For example, the mountain wave tends to steepen when it propagates to the region below a jet stream or a jet streak since the basic wind speed increases there. Note that in applying (5.2.27) to solve the problem, and in neglecting the last term of (5.2.28), we have implicitly adopted

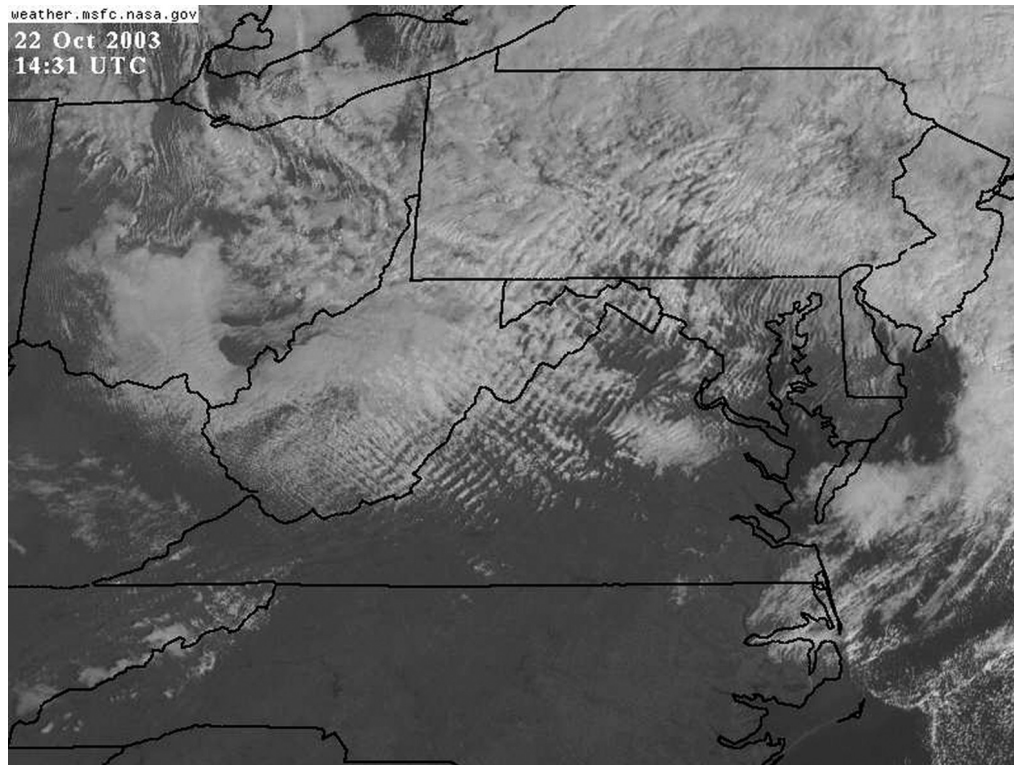


Fig. 5.6 Satellite imagery for lee wave clouds observed at 1431 UTC October 22, 2003 over western Virginia. Clouds originate at the Appalachian Mountains. (Courtesy of NASA.)

a first-order WKBJ (Wentzel–Kramers–Brillouin–Jeffreys) approximation. A second-order WKBJ approximation has been used to calculate wind profile effects on mountain wave drag (e.g., Teixeira and Miranda 2006). It is necessary to extend the WKBJ approximation to second order for these effects to be taken into account.

Based on (5.2.32) and previous discussions, waves may amplify in certain layers due to: (a) weaker stratification, (b) stronger wind, such as a jet stream or jet streak, (c) nonlinear steepening, and (d) abrupt decrease in the mean density, leading to an increase of $\sqrt{\rho_s/\rho(z)}$, in (5.2.12).

5.2.3 *Trapped lee waves*

One of the most prominent features of mountain waves is the long train of wave clouds over the lee of mountain ridges in the lower atmosphere, such as those shown in Fig. 5.6. This type of wave differs from the dispersive tails in Fig. 5.4 in that it is located in the lower atmosphere and there is no vertical phase tilt. It will be shown below that this type of trapped lee waves, or resonance waves, occurs when the Scorer parameter decreases rapidly with height (Scorer 1949).

The dynamics of trapped lee waves may be understood by considering a two-layer stratified fluid system. The wave equations for the vertical displacement in Fourier space may be written in a form similar to (5.2.1),

$$\hat{\eta}_{zz} + (\ell_1^2 - k^2)\hat{\eta} = 0 \text{ for } -H \leq z < 0 \text{ and} \quad (5.2.33a)$$

$$\hat{\eta}_{zz} - (k^2 - \ell_2^2)\hat{\eta} = 0 \text{ for } 0 \leq z. \quad (5.2.33b)$$

In this two-layer fluid system, we have assumed that $\ell_2^2 < k^2 < \ell_1^2$. For convenience, the ground and the interface of the lower and upper layers are assumed to be located at $z = -H$ and $z = 0$, respectively. The free wave solutions may be written as

$$\hat{\eta}_1(k, z) = C \left[\cos \mu z - \frac{\lambda}{\mu} \sin \mu z \right] \text{ and} \quad (5.2.34a)$$

$$\hat{\eta}_2(k, z) = C e^{-\lambda z}, \quad (5.2.34b)$$

where $\mu = \sqrt{\ell_1^2 - k^2}$, $\lambda = \sqrt{k^2 - \ell_2^2}$ and C is a constant coefficient to be determined by the lower boundary condition. The boundedness upper boundary condition has been applied to exclude the $\exp(\lambda z)$ term, and the kinematic and dynamic boundary conditions at the interface, i.e. the continuities of \hat{w} and \hat{w}_z at $z = 0$, have also been applied. Without enforcing a lower boundary condition, (5.2.34) represents free waves associated with this two-layer fluid system. The resonance waves are obtained by seeking the zeros of (5.2.34a) with $z = -H$,

$$\cot \mu H = -\lambda/\mu. \quad (5.2.35)$$

The resonance wave number (k_r^*) may be obtained by solving the above equation either numerically or graphically. The criterion for the existence of one or more resonance waves may be obtained (Scorer 1949):

$$\ell_1^2 - \ell_2^2 \geq \frac{\pi^2}{4H^2}. \quad (5.2.36)$$

A more general criterion for resonance waves of the n th mode is

$$\left[\frac{(2n+1)\pi}{2H} \right]^2 \geq (\ell_1^2 - \ell_2^2) \geq \left[\frac{(2n-1)\pi}{2H} \right]^2. \quad (5.2.37)$$

The above criterion implies that *in order to have resonance (lee) waves, the Scorer parameter in the lower layer must be much greater than that in the upper layer*. In other words, the lower layer must be more stable or with a much slower basic wind speed than the upper layer.

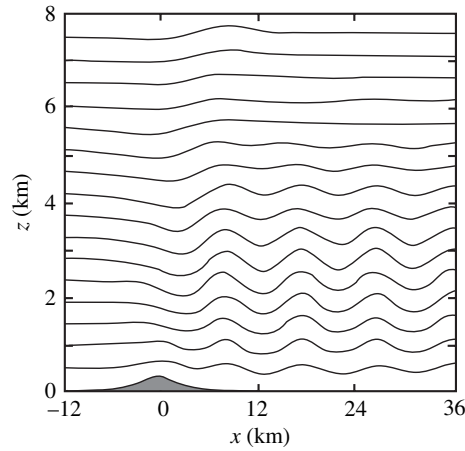


Fig. 5.7 Lee waves simulated by a nonlinear numerical model for a two-layer airflow over a bell-shaped mountain. Displayed are the quasi-steady state streamlines. In the lower layer (below 5 km approximately) $l^2 = 9 \times 10^{-7} \text{ m}^{-2}$, while in the upper layer, $l^2 = 2 \times 10^{-7} \text{ m}^{-2}$. (Adapted after Durran 1986b.)

In order to obtain a complete solution of the boundary value problem for a specific obstacle, we may apply the linear lower boundary condition,

$$\hat{\eta}_1(k, -H) = \hat{h}(k). \quad (5.2.38)$$

Substituting the above equation into (5.2.34) and taking the inverse Fourier transform of $\hat{\eta}(k, z)$ leads to the forced wave solution in the lower layer,

$$\eta_1(x, z) = 2\text{Re} \int_0^\infty \frac{\hat{h}(k)(\cos \mu z - (\lambda/\mu) \sin \mu z) e^{ikx}}{(\cos \mu H + (\lambda/\mu) \sin \mu H)} dk. \quad (5.2.39)$$

The singularity in the denominator of the above equation corresponds to the resonance mode that will produce lee waves. Equation (5.2.39) can be solved asymptotically or numerically with a given mountain-shape function (Scorer 1949; Smith 1979). Figure 5.7 shows lee waves simulated by a nonlinear numerical model for a two-layer airflow over a bell-shaped mountain. Due to the co-existence of the upward propagating waves and downward propagating waves, there exists no phase tilt in the lee waves.

Once lee waves form, regions of reversed cross-mountain winds near the surface beneath the crests of the lee waves may develop due to the presence of a reversed pressure gradient force. In the presence of surface friction, a sheet of vorticity parallel to the mountain range forms along the lee slopes, originates in the region of high shear within the boundary layer. The vortex sheet separates from the surface, ascends into the crest of the first lee wave, and remains aloft as it is advected downstream by the undulating flow in the lee waves (Doyle and Durran 2004). The vortex with recirculated air is known as *rotor* and the process that forms it is known as *boundary layer*

separation, which will be further discussed in Subsection 5.4.2 along with lee vortices. These rotors are often observed to the lee of steep mountain ranges such as over the Owens Valley, California, on the eastern slope of Sierra Nevada (e.g., Grubišić and Lewis 2004). Occasionally, a turbulent, altocumulus cloud forms with the rotor and is referred to as *rotor cloud*.

5.3 Nonlinear flows over two-dimensional mountains

As discussed in Sections 5.1 and 5.2, the response of a stably stratified flow over a two-dimensional mountain ridge has been studied extensively since the 1960s. In particular, the linear dynamics are fundamentally understood, especially due to the development of linear theories in earlier times. Linear theory, however, begins to break down when the perturbation velocity (u') becomes large compared with the basic flow (U) in some regions, so that the flow becomes stagnant. This happens when the mountain becomes very high, the basic flow becomes very slow, or the stratification becomes very strong. In other words, flow becomes more nonlinear when the Froude number, $F = U/Nh$, becomes small. For simplicity, the mountain height is denoted by h . Thus, in order to fully understand the dynamics of nonlinear phenomena, such as upstream blocking, wave breaking, severe downslope winds and lee vortices, we need to take a nonlinear approach. Note that the reciprocal of the Froude number, Nh/U , has also been used as a control parameter and is known as *nondimensional mountain height*. In the text, we will use these two parameters interchangeably.

Nonlinear response of a continuously stratified flow over a mountain is very complicated since the nonlinearity may come from the basic flow characteristics, the mountain height, or the transient behavior of the internal flow, such as wave steepening. In this section, we will begin with the discussion of a nonlinear theory developed by Long (1953), then discuss the two-dimensional flow regimes for a continuously stratified flow over a two-dimensional mountain with the help of nonlinear numerical models, and the generation mechanisms of severe downslope winds and wave breaking.

5.3.1 Nonlinear flow regimes

The governing equation for the finite-amplitude, steady state, two-dimensional, inviscid, continuously and stably stratified flow may be derived (Long 1953)

$$\nabla^2 \delta + \frac{1}{e} \frac{de}{dz} \left[\frac{\partial \delta}{\partial z} - \frac{1}{2} (\nabla \delta)^2 \right] + \frac{N^2}{U^2} \delta = 0, \quad (5.3.1)$$

where $\delta(x, z) = z - z_0$ is the streamline deflection at (x, z) from its far upstream, undisturbed height z_0 ; U and N are the far upstream basic flow speed and Brunt–Vaisala frequency, respectively, at height z_0 , and $e = (1/2)\rho_0 U^2$ is the kinetic energy of the upstream flow. In deriving (5.3.1), it has been assumed that there is no

streamline deflection far upstream. In order to solve the above nonlinear equation, (5.3.1), we must specify e . Under the special situation $de/dz = 0$ and when the flow is Boussinesq, which assumes that ρ is approximately constant and $U(z)$ and $N(z)$ are effectively constant, (5.3.1) becomes a linear *Helmholtz equation*,

$$\nabla^2 \delta + l^2 \delta = 0, \quad (5.3.2)$$

where $l = N/U$ is the Scorer parameter of the basic flow far upstream. The nonlinear lower boundary condition for (5.3.2) is given by

$$\delta(x, z) = h(x) \quad \text{at} \quad z = h(x), \quad (5.3.3)$$

where $h(x)$ is the height of the mountain surface. In other words, the nonlinear lower boundary condition is applied on the mountain surface, instead of approximately applied at $z = 0$ as in the linear lower boundary condition, such as (5.1.10). Equation (5.3.2) with the lower boundary condition (5.3.3) forms Long's model, in which the steady-state nonlinear flow is remarkably described by a linear differential equation with constant coefficients. In fact, (5.3.2) is exactly the same differential equation which applies to infinitesimal perturbations adopted in many linear theories and discussed earlier in this chapter. The appropriate upper boundary condition for a semi-infinite fluid, such as the atmosphere, is the radiation or boundedness condition, similar to (5.2.3) in the Fourier space for a uniform basic flow over an infinitesimal mountain.

Following the procedure for treating linear flow over small-amplitude mountains, we make the Fourier transform of (5.3.2),

$$\hat{\delta}_{zz} + (l^2 - k^2)\hat{\delta} = 0. \quad (5.3.4)$$

The general solution for the above equation is

$$\hat{\delta} = \hat{\delta}(k, 0)e^{imz} \quad \text{for} \quad l > k \quad \text{and} \quad (5.3.5a)$$

$$\hat{\delta} = \hat{\delta}(k, 0)e^{-\lambda z} \quad \text{for} \quad l < k, \quad (5.3.5b)$$

where $m = \sqrt{l^2 - k^2}$, and $\lambda = \sqrt{k^2 - l^2}$. Note that the upper radiation and boundedness conditions have been applied to (5.3.5a) and (5.3.5b), respectively, while the linear lower boundary condition has been applied at $z = 0$, instead of at $z = h(x)$. The streamline deflection in the physical space can then be obtained by taking the inverse Fourier transform

$$\delta(x, z) = \text{Re} \left[\int_0^l \hat{\delta}(k, 0)e^{imz} e^{ikx} dk + \int_l^\infty \hat{\delta}(k, 0)e^{-\lambda z} e^{ikx} dk \right], \quad (5.3.6)$$

which may be obtained numerically, as with the Fast Fourier Transform numerical technique. Other dynamical variables may be derived,

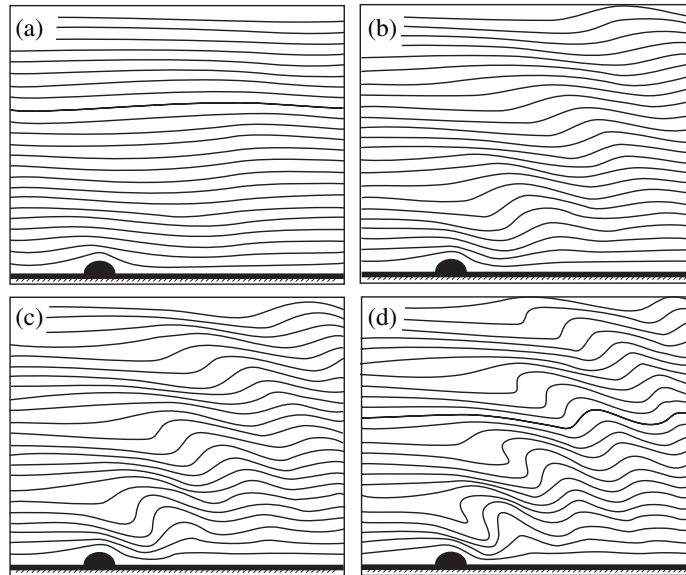


Fig. 5.8 Streamlines of Long's model solutions for uniform flow over a semi-circle obstacle with $Nh/U =$ (a) 0.5, (b) 1.0, (c) 1.27, and (d) 1.5, where Nh/U is the nondimensional mountain height. Note that the streamlines become vertical in (c) and overturn in (d). (Adapted from Miles 1968.)

$$u = \frac{\partial \psi}{\partial z}; w = -\frac{\partial \psi}{\partial x}; \rho = \rho_0 \left(1 - \frac{N^2}{gU} \psi \right); N^2 = -\frac{g}{\rho_0} \frac{\partial \rho}{\partial z}, \quad (5.3.7)$$

where ψ is the streamfunction defined as $U(z - \delta)$. The exact nonlinear lower boundary condition, (5.3.3), can be implemented using an iterative method (e.g., Laprise and Peltier 1989a).

Figure 5.8 shows streamlines of analytical solutions for flow over a semi-circle obstacle for the nondimensional mountain heights $Nh/U = 0.5, 1.0, 1.27,$ and 1.5 . As mentioned earlier, the nondimensional mountain height is a measure of the nonlinearity of the continuously stratified flow, which equals the reciprocal of the Froude number (U/Nh). When Nh/U is small, such as $Nh/U = 0.5$, the flow is more linear. When Nh/U increases to 1.27, the flow becomes more nonlinear and its streamlines become vertical at the first level of wave steepening. For flow with $Nh/U > 1.27$, the flow becomes statically and shear unstable (Laprise and Peltier 1989b). The vertical streamline marks the approximate limit of applicability of Long's model. For the hydrostatic solution of Long's model with a bell-shaped mountain subject to a nonlinear lower boundary condition, this critical value is $Nh/U = 0.85$ (Miles and Huppert 1969). Thus, for a continuously stratified, hydrostatic flow over a bell-shaped mountain, the flow may be classified as supercritical flow when $U/Nh > 1.18$ ($Nh/U < 0.85$) and as subcritical flow when $U/Nh < 1.18$ ($Nh/U > 0.85$). Note that in the literature it is often misquoted $U/Nh = 1$ as the regime boundary for supercritical and subcritical regimes for continuously stratified flow over mountains.

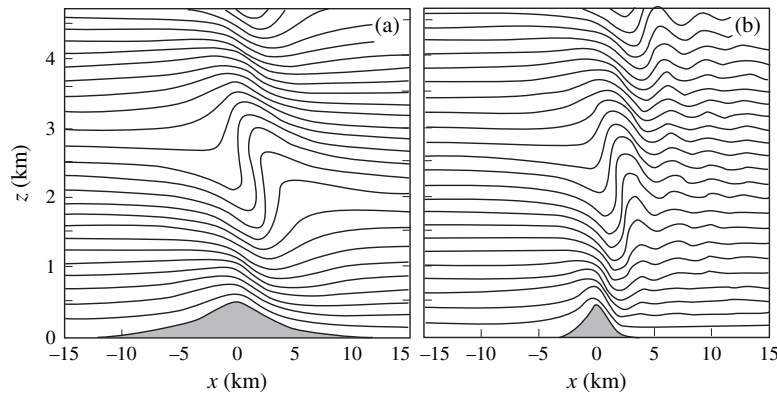


Fig. 5.9 (a) Streamlines for Long's model solution over a bell-shaped mountain with $U = 5 \text{ m s}^{-1}$, $N = 0.01 \text{ s}^{-1}$, $h_m = 500 \text{ m}$ and $a = 3 \text{ km}$; and (b) same as (a) except with $a = 1 \text{ km}$. An iterative method is applied in solving the nonlinear equation (5.3.2) with the nonlinear lower boundary condition (5.3.3) applied. Note that the dispersive tail of the nonhydrostatic waves is present in the narrower mountain case (case(b)). (Adapted from Laprise and Peltier 1989a.)

As discussed in Section 3.3, there exist five flow regimes in a one-layer shallow-water system, based on the shallow water Froude number, $F = U/\sqrt{gH}$, and the nondimensional mountain height, $M = h_m/H$ (Fig. 3.3). In a nonrotating, continuously stratified flow over a two-dimensional, bell-shaped mountain, three nondimensional control parameters may be identified: U/Nh , h/a , and Na/U . However, only two of them are independent. The parameter h/a measures the steepness of mountain, and Na/U is the nondimensional mountain width which measures the degree of hydrostatic effect (the larger the more hydrostatic). In the hydrostatic limit ($Na/U \rightarrow \infty$), the sole control parameter is the Froude number.

Figure 5.9a shows streamlines for Long's model for flow over a bell-shaped mountain with a half-width (a) of 3 km with the nonlinear lower boundary condition (5.3.3) applied. Internal waves tend to overturn in regions of reversed density gradient (statically unstable), $\partial\rho/\partial z > 0$, which corresponds to $\partial\delta/\partial z > 1$ from (5.3.7). The heights of critical steepening levels differ slightly from those predicted by linear theory for hydrostatic waves, $z_o = (n + 3/4)(2\pi U/N)$, where n is an integer, just over the crest of the topography (Laprise and Peltier 1989a). In Fig. 5.9a, the first steepening level for nonlinear, hydrostatic waves is about 2.36 km. With a narrower mountain, such as $a = 1 \text{ km}$ (Fig. 5.9b), a dispersive tail, caused by nonhydrostatic dispersion, is produced. The downstream displacement of the steepened region is caused by both the nonhydrostatic effect and the nonlinearity of the interior flow and the lower boundary condition. When $Na/U \gg 1$, the flow approaches the hydrostatic limit. This control parameter can be obtained by comparing the scales of $\partial^2 w'/\partial x^2$ and $N^2 w'/U^2$ of (5.1.5). Direct comparison of $\partial^2 w'/\partial x^2$ and $\partial^2 w'/\partial z^2$ terms by scale analysis leads to the conclusion that h/a is a control parameter of nonhydrostatic effect. The Froude number, U/Nh , can also be derived by comparing the scales of $\partial^2 w'/\partial z^2$ and $N^2 w'/U^2$ of (5.1.5).

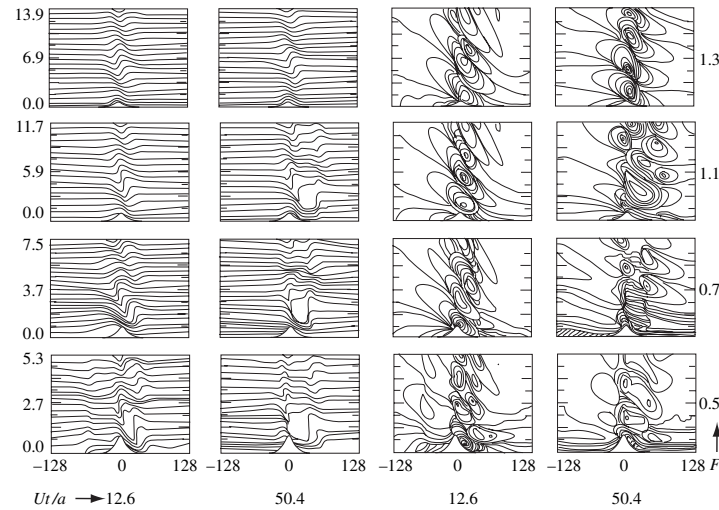


Fig. 5.10 Nonlinear flow regimes for a two-dimensional, hydrostatic, uniform flow over a bell-shaped mountain as simulated by a numerical model, based on the Froude number ($F = U/Nh$). F varies from 0.5 to 1.3, which gives four different flow regimes as discussed in the text. Displayed are the θ fields (left two columns) and the u' fields (right two columns) for two nondimensional times $Ut/a = 12.6$ and 50.4 . The dimensional parameters are: $N = 0.01 \text{ m s}^{-1}$, $h = 1 \text{ km}$, $a = 10 \text{ km}$, and $U = 5, 7, 11,$ and 13 m s^{-1} corresponding to $F = 0.5, 0.7, 1.1,$ and 1.3 , respectively. A constant nondimensional physical domain height of $1.7\lambda_z$ (where $\lambda_z = 2\pi U/N$) is used. Both the abscissa and ordinate in the small panels are labeled in km. (Adapted after Lin and Wang 1996.)

Long's nonlinear theory advances our understanding of orographically forced flow considerably. However, the constant upstream condition assumed by Long may not be necessarily consistent with the flow established naturally by transients, especially when blocking occurs (Garner, 1995). In the real atmosphere, turbulence will come into play and produce vertical mixing in a subcritical (overturning) flow. To simulate a subcritical flow, one may consider using a laboratory tank experiment or adopting a nonlinear numerical model. As mentioned earlier, flow may become stagnant, where the total horizontal wind speed reduces to zero, in essentially two regions: in the interior of the fluid over the mountaintop or on the lee slope and along the upstream slope of the mountain.

Flow stagnation in a two-dimensional flow is responsible for *flow recirculation*, while stagnation in a three-dimensional flow is responsible for *flow splitting*. Flow stagnation in the interior of the fluid is due to nonlinear *wave steepening*, which may lead to *wave breaking* and *wave overturning* over the lee slope, while the flow stagnation at the upstream surface of the mountain is called *flow blocking*. Although the two-dimensional, nonrotating, hydrostatic flow may be simply classified as supercritical and subcritical regimes, as discussed above, the transient flow behavior becomes much more complicated. Figure 5.10 shows the time evolution for the θ and u' fields for a hydrostatic flow over a two-dimensional, bell-shaped mountain

simulated by a numerical model at nondimensional times $Ut/a = 12.6$ and 50.4 for F ranging from 0.5 to 1.3 . Four regimes are identified: (I) flow with neither wave breaking aloft nor upstream blocking (e.g., $1.12 \leq F$), (II) flow with wave breaking aloft in the absence of upstream blocking (e.g., $0.9 \leq F < 1.12$), (III) flow with both wave breaking and upstream blocking, but where wave breaking occurs first (e.g., $0.6 \leq F < 0.9$), and (IV) flow with both wave breaking and upstream blocking, but where blocking occurs first (e.g., $0.3 \leq F < 0.6$). Note that the exact Froude numbers separating these flow regimes might be different in other numerically simulated results because these numbers are sensitive to some numerical factors, such as the grid resolution, domain size, numerical boundary conditions, and numerical scheme adopted in different numerical models.

In regime I (e.g., $F = 1.3$ in Fig. 5.10), neither wave breaking nor upstream blocking occurs, but an upstream propagating *columnar disturbance* does exist. The basic flow structure in regime I resembles linear mountain waves. Columnar disturbances are wave modes with constant phase in the vertical, which permanently alter the upstream temperature and horizontal velocity fields as they pass through the fluid (e.g., Pierrehumbert and Wyman 1985). A columnar disturbance may be generated by a sudden imposition of a disturbance, such as the impulsive introduction of a mountain in a uniform flow. Regime II (e.g., $F = 1.1$ in Fig. 5.10) resembles weakly nonlinear mountain waves. In this flow regime, an internal jump forms at the downstream edge of the wave-breaking region above the mountain, propagates downstream, and then becomes quasi-stationary. The region of wave breaking also extends downward toward the lee slope. After the internal jump travels farther downstream, a stationary mountain wave becomes established in the vicinity of the mountain above the dividing streamline, which is induced by wave breaking. A high-drag state is predicted in this flow regime. In addition, a vertically propagating hydrostatic gravity wave is generated by the propagating jump and travels with it. Along the lee slope, a strong downslope wind develops. Static and shear instabilities may occur locally in the region of wave breaking. The computed critical Froude number for wave breaking is about 1.12 , which agrees well with the value 1.18 found by Miles and Huppert (1969).

In regime III (e.g., $F = 0.7$ in Fig. 5.10), the internal jump over the lee slope propagates downstream in the early stage and then becomes quasi-stationary. Note that the propagation of the downstream internal jump is sensitive to the upstream numerical boundary condition, which may cause the internal jump to retrogress upstream. To avoid this artificial effect from the numerical model, the upstream boundary should be placed far enough so as to effectively reduce its impact. Also, the layer depth of blocked fluid upstream is independent of the Froude number. In regime IV (e.g., $F = 0.5$ in Fig. 5.10), a significant portion of the upstream flow is blocked by the mountain. The presence of wave breaking aloft is not a necessary condition for upstream blocking to occur. A vertically propagating gravity wave is generated by the upstream reversed flow and travels with it. The speed of the upstream

reversed flow is proportional to h/a . The surface drag increases abruptly from regime I to II, while it decreases gradually from regime II (III) to III (IV).

Flow regimes may also be classified in different ways, depending upon particular characteristics. For example, two-dimensional, uniform flow over an isolated mountain has been classified as either a quasi-linear regime, high-drag state, or blocked state, based on Nh/U and NU/g (Stein 1992). In addition, the flow response of a three-dimensional flow over a long ridge is very different from that of a two-dimensional flow when Nh/U is large. For example, the onset of wave breaking and the transition to the high-drag state in the three-dimensional flow was found to be accompanied by an abrupt increase in deflection of the low-level flow around the ridge (Epifanio and Durran 2001). The increased flow deflection is produced at least in part by upstream-propagating columnar disturbances forced by the transition to the high-drag state.

5.3.2 Generation of severe downslope winds

Severe downslope winds over the lee of a mountain ridge have been observed in various places around the world, such as the *chinook* over the Rocky Mountains, *foehn* over the Alps, *bora* over the Dinaric Alps, *zonda* over the Argentina mountains, *berg wind* in South Africa, *Canterbury-nor'wester* in New Zealand, *halny wiatr* in the mountains of Poland, *Santa Ana winds* in southern California, and *Diabolo winds* in San Francisco Bay Area. One well-known event is the January 11, 1972 windstorm which occurred in Boulder, Colorado, and which reached a peak wind gust as high as 60 m s^{-1} and produced severe damage in the Boulder area (Fig. 3.4a).

The basic dynamics of the severe downslope wind can be understood from the following two major theories: (a) *resonant amplification theory* (Clark and Peltier 1984), and (b) *hydraulic theory* (Smith 1985), along with later studies on the effects of instabilities, wave ducting, nonlinearity, and upstream flow blocking. These will be reviewed in the following.

a. Resonant amplification theory

Idealized nonlinear numerical experiments indicate that a high-drag (severe-wind) state occurs after an upward propagating mountain wave breaks above a mountain, such as happens in Fig. 5.10 ($F=0.5, 0.7, \text{ and } 1.1$), in which severe downslope winds develop in a uniform flow over a bell-shaped mountain. The wave-breaking region is characterized by strong turbulent mixing (where $R_i < 0.25$), with a local wind reversal on top of it. As mentioned in Section 3.8, the *wind reversal level* coincides with the critical level for a stationary mountain wave, and thus is also referred to as the *wave-induced critical level*. The lowest wave-induced critical level starts to develop at the height $z = 3\lambda_z/4 \approx 2.36, 3.30, \text{ and } 5.18 \text{ km}$ for cases of $F=0.5, 0.7, \text{ and } 1.1$, respectively (at $U/a = 12.6$ in Fig. 5.10), where $\lambda_z (= 2\pi U/N)$ is the hydrostatic vertical wavelength. A supercritical

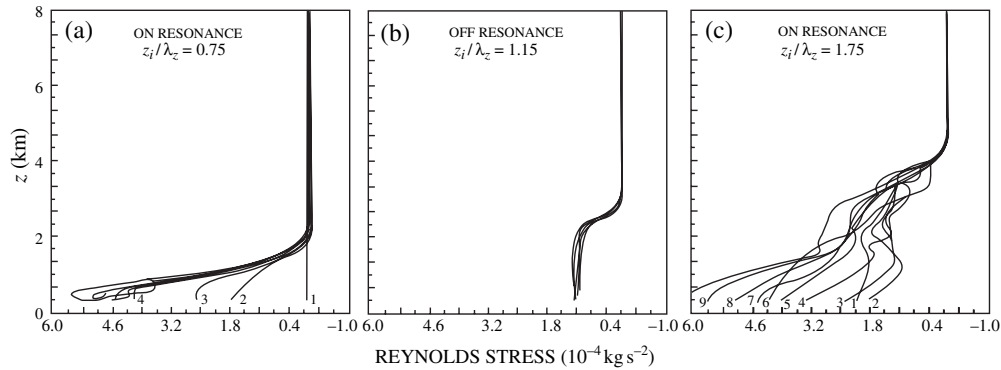


Fig. 5.11 Resonant amplification mechanism for severe downslope winds developed for basic flow with a prescribed critical level (z_i) over a bell-shaped mountain. Displayed are the evolution of the Reynolds stress, $\langle \rho_o u' w' \rangle$, profile for on-resonance flows with: $z_i/\lambda_z =$: (a) 0.75 and (c) 1.75 and for the off-resonance flow with (b) $z_i/\lambda_z = 1.15$, where $\lambda_z = 2\pi U_o/N$. The flow and orographic parameters are: $N = 0.02 \text{ s}^{-1}$, $U(z) = U_o \tanh[(z - z_i)/b]$ with $U_o = 8 \text{ m s}^{-1}$, $b = 600 \text{ m}$, $R_{\min} = N^2/(U_o/b)^2 = 2.25$ (minimum R_i), $h = 300 \text{ m}$, and $a = 3 \text{ km}$. The Froude number (U_o/Nh) is 1.33. Height (z) is in km. The profiles in the figure range in time from 0 to $2880\Delta t$, 1440 to $2880\Delta t$, and 2080 to $4240\Delta t$ for panels (a) to (c), respectively, where $\Delta t = 5 \text{ s}$. Some of the profiles are sequentially numbered from earliest to latest (labeled by small numbers). (After Clark and Peltier 1984.)

flow with a severe downslope wind can be found over the lee slope under the wave breaking region, which undergoes a transition from subcritical flow over the upwind slope. The maximum perturbation wind over the lee slope is much higher than those predicted by linear and weakly nonlinear theories. At a later stage, the *well-mixed layer* (*wake*) deepens, the depth of *internal hydraulic jump* (*critically steepened streamlines*) extends to a great depth, the flow above the initial wave-induced critical level is less disturbed compared to that in the lower layer, and severe winds develop over the lee slope and below the well-mixed layer ($Ut/a = 50.4$ in Fig. 5.10).

The above example implies that the wave breaking region aloft acts as an internal boundary which reflects the upward propagating waves back to the ground and produces a high-drag state through partial resonance with the upward propagating mountain waves. This is shown by performing nonlinear numerical simulations for stratified flow over a bell-shaped mountain (Fig. 5.11). In these simulations, the basic flow reverses its direction at a prescribed critical level (z_i). In the absence of shear instability associated with the basic flow, and when the basic-flow critical level is located at a nondimensional height of $z_i/\lambda_z = 3/4 + n$ (n is an integer) above the surface, nonlinear resonant amplification occurs between the upward propagating waves generated by the mountain and the downward propagating waves reflected from the critical level. This leads to an extremely large Reynolds stress or surface drag and severe downslope winds (Figs. 5.11a and 5.11c). In other words, the flow is *on resonance*. On the other hand, when the basic flow critical level is located at a

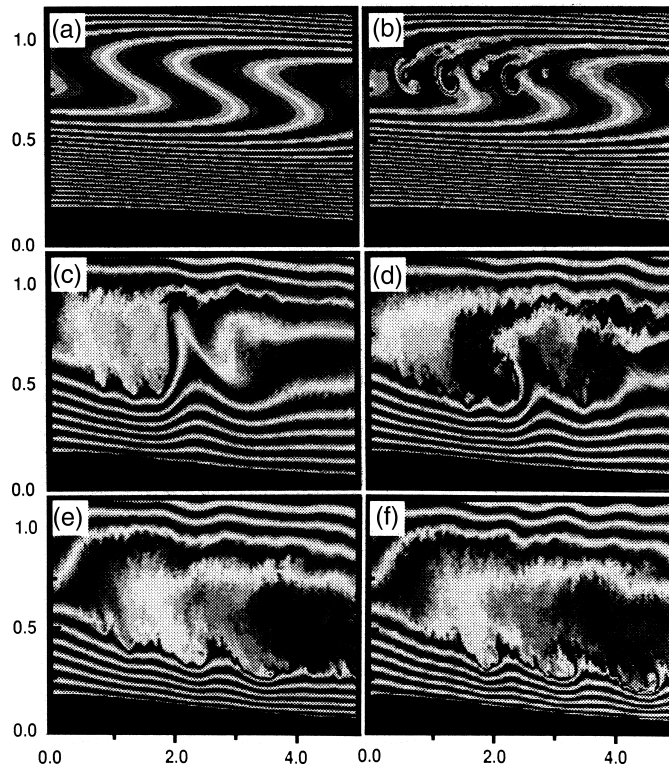


Fig. 5.12 Three distinct stages for the development of severe downslope winds, as revealed by the triply-nested numerical solutions. See text for details. Long's (1953) nonlinear analytical solution is used to initiate the flow. Displayed are the potential temperature fields over the lee slope at model times of (a) 0, (b) 20, (c) 66, (d) 96, (e) 160, and (f) 166 min. The grid resolutions for the outer, middle, and inner domains are 500 m, 50 m, and $16^{2/3}$ m respectively. A bell-shaped mountain with $h = 165$ m and $a = 3$ km is used. The upstream flow parameters are $U = 3.3 \text{ m s}^{-1}$ and $N = 0.02 \text{ s}^{-1}$. Thus, $F = U/Nh = 1$. (Adapted after Scinocca and Peltier 1993.)

nondimensional height off $z_i/\lambda_z = 3/4 + n$, such as 1.15, there is no wave resonance and no severe downslope winds generated (Fig. 5.11b). Because the severe downslope winds are developed by resonance between upward and downward waves, this mechanism is referred to as the *resonant amplification mechanism*.

Based on numerical simulations with finer-grid resolutions, three distinct stages for the development of severe downslope winds are identified (Scinocca and Peltier 1993). (1) Local static (buoyancy) instability develops when the wave steepens and overturns, thus producing a pool of well-mixed air aloft (Figs. 5.12a–b). (2) A well-defined large-amplitude stationary disturbance is generated over the lee slope. In time, small-scale secondary Kelvin–Helmholtz (K–H) (shear) instability develops in local regions of enhanced shear associated with flow perturbations caused by the large-amplitude disturbance (Figs. 5.12c–d). (3) The region of enhanced wind on the lee slope expands downstream, eliminating the perturbative structure associated with the large-amplitude

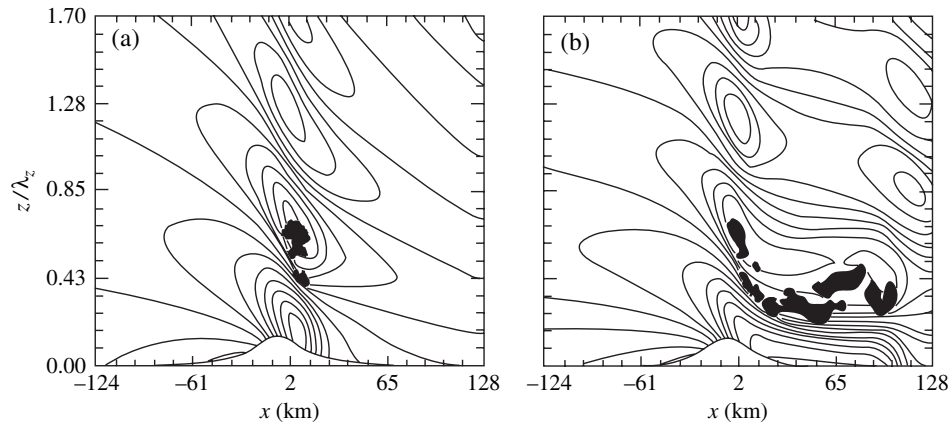


Fig. 5.13 Wave ducting as revealed by the time evolution of horizontal wind speeds and regions of local $R_i < 0.25$ (shaded) for a flow with uniform wind and constant static stability over a mountain ridge at $U_1/a =$ (a) 12.6, and (d) 50.4. The Froude number of the uniform basic wind is 1.0. (Adapted after Wang and Lin 1999.)

stationary disturbance (Figs. 5.12e–f). The K–H instability dominates the flow in this mature windstorm state. Thus, static instability helps explain the initiation of wave-induced critical level and the downstream expansion of the severe downslope winds.

Once wave breaking occurs, it induces a critical level in the shear layer with low R_i and thus establishes a flow configuration favorable for *wave ducting* in the lower uniform flow layer, similar to that in case 3 of Table 4.1 and Fig. 4.12b. Effects of the wave ducting on the development of high-drag states for a flow with uniform wind and constant static stability are illustrated in Fig. 5.13. Shortly after the occurrence of wave breaking, regions with local $R_i < 0.25$ form in the vicinity of the wave breaking (Fig. 5.13a). This turbulent mixing region is expanding downward and downstream due to strong nonlinear effects on the flow with low Richardson number near the critical level (Fig. 5.14a). The turbulent mixing region expands downward by wave reflection, overreflection, and ducting from the wave-induced critical level and accelerates downstream by the nonlinear advection (Fig. 5.13b).

Effects of wave reflection and/or overreflection are evidenced by the fact that the wave duct with severe downslope wind is located below the region of the turbulent mixing region. Note that the expansion of the turbulent mixing region provides a maintenance mechanism for the existence of the wave duct below it and above the lee slope, because the reflectivity in this region is about 1 according to linear theory. Without this almost perfect reflector, the wave below cannot be maintained and would lose most of its energy due to dispersion. In fact, wave overreflection can occur, according to the wave ducting theory discussed in Chapter 4, through the extraction energy from the well-mixed region and thus contribute to the acceleration of downslope winds. In the absence of nonlinearity (Fig. 5.14b), the wavebreaking region does not expand downward to reduce the depth of the lower uniform wind layer. This, in

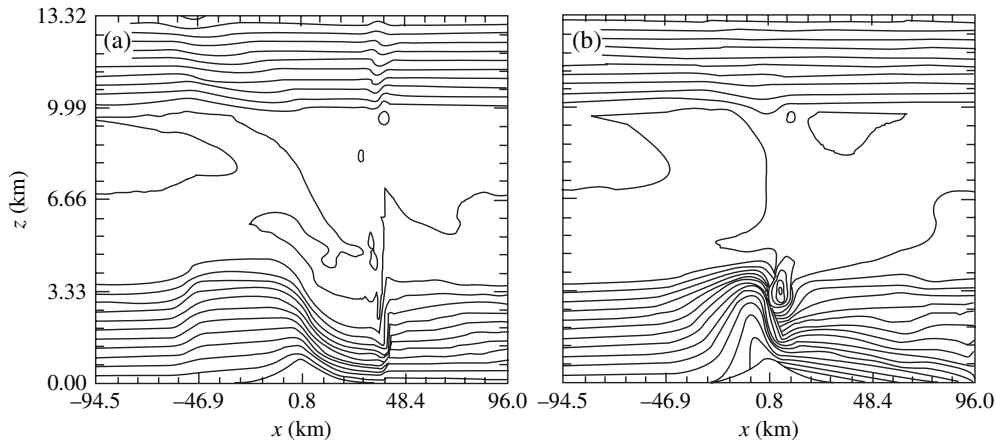


Fig. 5.14 Effects of nonlinearity on the development of severe downslope winds: (a) Potential temperature field from nonlinear numerical simulations for a basic flow with $R_f = 0.1$ and $F = 2$; (b) Same as (a) except from linear numerical simulations. The contour interval is 1 K in both (a) and (b). (Adapted after Wang and Lin 1999.)

turn, prohibits the formation of the severe downslope wind and internal hydraulic jump. These results indicate that the nonlinear wave ducting has contributed to the downward and downstream expansion of the turbulent mixing region.

b. Hydraulic theory

Based on the similarity of flow configurations of severe downslope windstorms and finite-depth, homogeneous flow over a mountain ridge, a hydraulic theory was proposed to explain the development of severe downslope winds (Smith 1985). The hydraulic theory attributes the high-drag (severe-wind) state to the interaction between a smoothly stratified flow and the deep, well-mixed, turbulent “dead” region above the lee slope in the middle troposphere. When a high-drag state develops, a *dividing streamline* encompasses this well-mixed region of uniform density (ρ_c in Fig. 5.15a). Assuming the upstream flow is uniform in U and N and the general flow is smooth, nondissipative, hydrostatic, Boussinesq and steady (Fig. 5.15a), the nonlinear, hydrostatic governing equation can be simplified from (5.3.2),

$$\delta_{zz} + f^2 \delta = 0, \quad (5.3.8)$$

The horizontal velocity can be derived from (5.3.7),

$$u = U(1 - \delta_z). \quad (5.3.9)$$

The lower boundary condition is given by (5.3.3). By assuming no disturbance above the upper dividing streamline (H_o), the pressure at $z = H_o$ is constant, i.e. $p(x, H_o) = p^*$. If the air in the turbulent region is hydrostatic in the mean and well mixed with a density

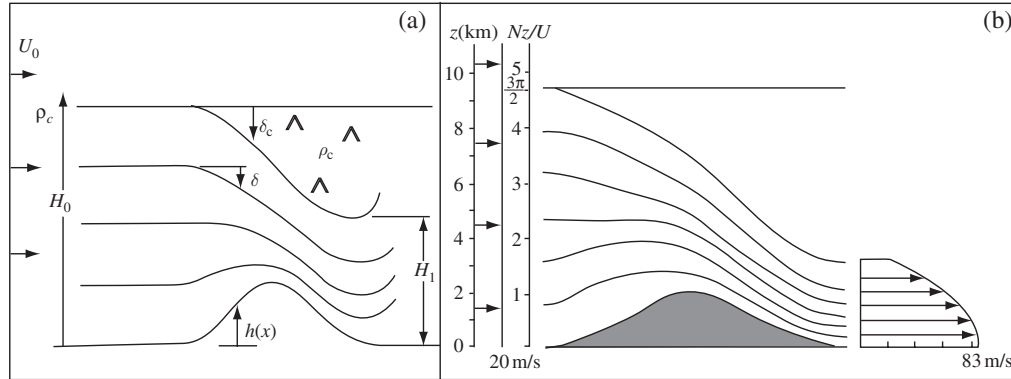


Fig. 5.15 A severe downslope windstorm simulated by a hydraulic theory. (a) Schematic of an idealized high-drag state flow configuration. A certain critical streamline divides and encompasses a region of uniform density (ρ_c), which is called the dividing streamline. H_0 and H_1 denote the heights of upstream dividing streamline and the downstream lower dividing streamline, respectively. (b) An example of transitional flow over a mountain. The dimensional values of the flow and orographic parameters are $U = 20 \text{ m s}^{-1}$, $N = 0.01 \text{ s}^{-1}$, $H_0 = 9.42 \text{ km}$, and $h = 2 \text{ km}$. This gives $F = U/Nh = 1$. (Adapted after Smith 1985.)

of ρ_c , the pressure along the lower branch of the dividing streamline is $p(x, H_0 + \delta_c) = p^* - \rho_c g \delta_c$, where δ_c is the vertical displacement of the lower dividing streamline (H_1). For a steady-state flow, the Bernoulli equation along $z = H_0 + \delta_c$ can be written

$$p + (1/2)\rho u^2 + \rho_c g z = \text{constant}. \quad (5.3.10)$$

At $z = H_0 + \delta_c$, we have

$$\delta_z = 0. \quad (5.3.11)$$

By assuming a wave-like solution in the vertical,

$$\delta(x, z) = A(x) \cos lz + B(x) \sin lz, \quad (5.3.12)$$

the nonlinear solution for high-drag state can be obtained,

$$\tilde{h} = \tilde{\delta}_c [\cos(\tilde{H}_0 + \tilde{\delta}_c - \tilde{h})], \quad (5.3.13a)$$

$$\tilde{A} = \tilde{\delta}_c \cos(\tilde{H}_0 + \tilde{\delta}_c), \text{ and} \quad (5.3.13b)$$

$$\tilde{B} = \tilde{\delta}_c \sin(\tilde{H}_0 + \tilde{\delta}_c), \quad (5.3.13c)$$

where $h(x)$ is the terrain height function and all coefficients and parameters are nondimensionalized by $l (= N/U)$ and denoted by tildes “ \sim ”. The above solution can be solved graphically or numerically as long as \tilde{h} and \tilde{H}_0 are known.

Figure 5.15 shows an example of a severe downslope windstorm simulated by a hydraulic theory with $F = 1$. The descent of the lower dividing streamline begins over the point where the mountain begins to rise and becomes more rapid over the mountain peak. The final downward displacement of the dividing streamline is a large fraction of the initial layer depth. The flow speed after transition to supercritical flow over the lee slope from subcritical flow over the upslope is greatest near the surface and is several times the upstream value. The flow shown in Fig. 5.15b is qualitatively similar to the 1972 Boulder windstorm observations (Fig. 3.4a). In addition to the above solution, the strength of the transitional flow can be measured by the pressure drag on the mountain per unit length,

$$\mathcal{D} = \frac{\rho_0 N^2}{6} (H_0 - H_1)^3. \quad (5.3.14)$$

The hydraulic theory of severe downslope winds was confirmed by numerical experiments of stratified fluid flow (e.g., Durran and Klemp 1987; Bacmeister and Pierrehumbert 1988) and laboratory tank experiments (e.g., Rottman and Smith 1989). Note that in order to apply the hydraulic theory to the prediction of the steady-state flow over a mountain, it is necessary to specify the initial height of the dividing streamline line. Thus, the dividing streamline height cannot be determined a priori if the critical level is induced by wave breaking. This, in turn, implies that the hydraulic model is limited to the consistent check of a severe wind state and cannot be used for prediction.

c. Applications of resonant amplification and hydraulic theories

Some discrepancies have been found between the resonant amplification and hydraulic theories of severe downslope windstorms. One discrepancy is the different critical level heights for high-drag (severe wind) states predicted by these two theories. The resonant amplification theory predicts the wave-induced critical (wave breaking) level at a height of $z/\lambda_z = 3/4 + n$ (n an integer), which helps produce severe downslope winds at later times. On the other hand, the hydraulic theory predicts critical level heights falling within the range of $z/\lambda_z = 1/4 + n$ to $3/4 + n$ during a high-drag state. This discrepancy appears to be caused by different stages of the severe downslope wind state being used for prediction. In fact, in earlier stages of a high-drag state, the resonant amplification theory is consistent with weakly nonlinear theories which indicate that the initiation of a high-drag transitional flow begins with linear resonance (Grimshaw and Smyth 1986), and with nonlinear numerical simulations which indicate that the lowest initial wave-induced critical level is near $3/4$ (Lin and Wang 1996). It can also be seen clearly from Fig. 5.10 that the wave-induced critical level for a severe-wind state is shifted to a lower level at later time. Therefore, it appears that the resonant amplification theory focuses on the earlier stage of severe downslope wind development, while the hydraulic theory focuses on the later stage.

Part of the discrepancies may be related to the usage of critical level height as the control parameter to determine a high-drag state, as often adopted in many previous

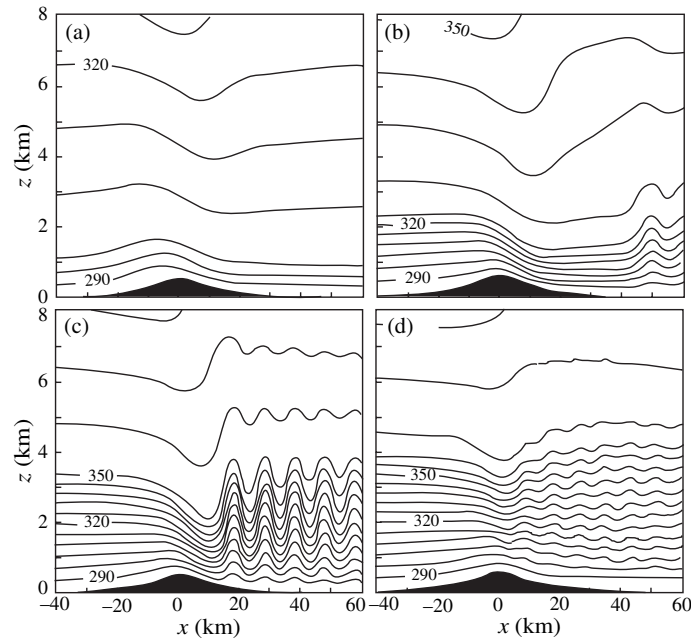


Fig. 5.16 The dependence of high-drag states on the lower-layer depth, as revealed by the isentropes for airflow in a two-layer atmosphere at $Ut/a = 25$, when $N_1 h/U = 0.5$, where N_1 is the Brunt–Vaisala frequency of the lower layer, and the depth of the lowest, most stable layer (U/N_1) is: (a) 1, (b) 2.5, (c) 3.5, and (d) 4. The lower layer resembles: (a) supercritical flow, (b) a propagating hydraulic jump, (c) a stationary jump, and (d) subcritical flow. (After Durran 1986a.)

studies. Based on some numerical experiments, the lower uniform flow layer depth appears to be a more appropriate scale to use (Wang and Lin 1999). Figure 5.16 indicates that the high-drag state is sensitive to the lower stable layer depth (Durran 1986a). Using the lower layer depth as the control parameter, predictions of both high- and low-drag states from several previous numerical studies are shown to be consistent, and the high-drag state does depend on the mountain height, which is consistent with the hydraulic theory. In addition, some discrepancies among previous studies result from the choice of different Richardson numbers and basic flow velocity profiles (e.g., Teixeira *et al.* 2005).

5.4 Flows over three-dimensional mountains

Although the two-dimensional mountain wave theories discussed in previous sections helped explain some important flow phenomena generated by infinitely long ridges, such as upward propagating mountain waves, lee waves, wave overturning and breaking, and severe downslope winds, in reality most of the mountains are of three-dimensional, complex form. The basic dynamics of flow over complex terrain can be understood by considering flow over an idealized, three-dimensional, isolated mountain. In this section,

we will discuss a linear theory of a stratified flow past an isolated mountain, as well as the generation of lee vortices in a nonlinear flow over an isolated mountain.

5.4.1 Linear theory

In the following, the two-dimensional, linear mountain wave theory developed in Section 5.2.1 is extended to three-dimensional flow over an isolated mountain. Consider a steady-state, small-amplitude, adiabatic, inviscid, nonrotating, stratified, Boussinesq fluid flow with uniform basic velocity (U) and Brunt–Vaisala frequency (N) over a three-dimensional topography $h(x, y)$. The governing linear equations can be derived from (5.1.1)–(5.1.4),

$$U \frac{\partial u'}{\partial x} + \frac{1}{\rho_0} \frac{\partial p'}{\partial x} = 0, \quad (5.4.1)$$

$$U \frac{\partial v'}{\partial x} + \frac{1}{\rho_0} \frac{\partial p'}{\partial y} = 0, \quad (5.4.2)$$

$$U \frac{\partial w'}{\partial x} - g \frac{\theta'}{\theta_0} + \frac{1}{\rho_0} \frac{\partial p'}{\partial z} = 0, \quad (5.4.3)$$

$$\frac{\partial u'}{\partial x} + \frac{\partial v'}{\partial y} + \frac{\partial w'}{\partial z} = 0, \quad (5.4.4)$$

$$U \frac{\partial \theta'}{\partial x} + \frac{N^2 \theta_0}{g} w' = 0. \quad (5.4.5)$$

Using (5.1.19), the above equations can be combined into a single equation of the vertical displacement (η),

$$\nabla^2 \eta_{xx} + \frac{N^2}{U^2} \nabla_H^2 \eta = 0. \quad (5.4.6)$$

Equation (5.4.6) can be solved by taking the double Fourier transform in x and y to obtain

$$\hat{\eta}_{zz} + m^2 \hat{\eta} = 0, \quad (5.4.7)$$

where

$$m^2 = K^2 (N^2 / k^2 U^2 - 1), \quad (5.4.8)$$

and $K = \sqrt{k^2 + l^2}$ is the horizontal wave number. The double Fourier transform pair is defined as

$$\hat{\eta}(k, l, z) = \frac{1}{4\pi^2} \int_{-\infty}^{\infty} \int_{-\infty}^{\infty} \eta(x, y, z) e^{-i(kx+ly)} dx dy, \text{ and} \quad (5.4.9a)$$

$$\eta(x, y, z) = \int_{-\infty}^{\infty} \int_{-\infty}^{\infty} \hat{\eta}(k, l, z) e^{i(kx+ly)} dk dl. \quad (5.4.9b)$$

The solution to (5.4.7) in the Fourier space can be found

$$\hat{\eta}(k, l, z) = \hat{\eta}(k, l, 0) e^{im(k,l)z}. \quad (5.4.10)$$

Similar to the two-dimensional mountain wave theory, as discussed in Section 5.2, there exist two flow regimes: (I) $N^2/k^2U^2 > 1$, and (II) $N^2/k^2U^2 < 1$. For upward propagating waves (regime I), the sign of m must be the same as the sign of k , in order to satisfy the upper radiation condition. On the other hand, for evanescent waves (regime II), the positive root of (5.4.8) must be chosen, i.e.

$$\hat{\eta}(k, l, z) = \hat{\eta}(k, l, 0) e^{-m_i(k,l)z}, \quad (5.4.11)$$

where m_i is defined as $K\sqrt{1 - N^2/k^2U^2}$. The linear lower boundary condition is

$$\eta(x, y, z = 0) = h(x, y), \quad (5.4.12)$$

which can be transformed into the Fourier space,

$$\hat{\eta}(k, l, 0) = \hat{h}(k, l). \quad (5.4.13)$$

From the definition of inverse Fourier transform and (5.4.13), we have

$$\eta(x, y, z) = \int_{-\infty}^{\infty} \int_{-\infty}^{\infty} \hat{h}(k, l) e^{im(k,l)z} e^{i(kx+ly)} dk dl. \quad (5.4.14)$$

Now let us consider a three-dimensional (circular) bell-shaped mountain

$$h(x, y) = \frac{h}{(r^2/a^2 + 1)^{3/2}}; \quad r = \sqrt{x^2 + y^2}, \quad (5.4.15)$$

where h and a are the mountain height and horizontal scale, respectively. The Fourier transform of (5.4.15) is,

$$\hat{h}(k, l) = \frac{ha^2}{2\pi} e^{-aK}. \quad (5.4.16)$$

The problem may be further simplified by using the hydrostatic approximation, i.e. neglecting the first term of (5.4.3). Note that under the hydrostatic approximation, we require that $Na/U \gg 1$. The solution, (5.4.14), may be reduced to a single integration by converting it into cylindrical coordinates, and asymptotic

solutions for the flow aloft and the flow near the ground may thus be obtained (Smith 1980). Substituting (5.4.16) into (5.4.14) and nondimensionalizing it according to

$$(\tilde{x}, \tilde{y}) = (x/a, y/a), (\tilde{z}, \tilde{\eta}) = (Nz/U, N\eta/U), (\tilde{k}, \tilde{l}, \tilde{K}) = (ka, la, Ka), \quad (5.4.17)$$

yields

$$\tilde{\eta}(\tilde{x}, \tilde{y}, \tilde{z}) = \frac{1}{F} \int_{-\infty}^{\infty} \int_{-\infty}^{\infty} e^{-\tilde{K}\tilde{z}} e^{i\tilde{m}\tilde{z}} e^{i(\tilde{k}\tilde{x} + \tilde{l}\tilde{y})} d\tilde{k}d\tilde{l}, \quad (5.4.18)$$

where F is the Froude number, as defined earlier. As discussed earlier, the linear theory holds for a large Froude number flow. On the other hand, for a small Froude number flow, nonlinear effects become more important and cannot be ignored. This will be discussed in the next subsection.

Equation (5.4.18) or (5.4.14) can also be solved numerically by applying a two-dimensional numerical FFT algorithm. Figure 5.17 shows an example of a linear hydrostatic flow passing over a bell-shaped mountain with a Froude number of 100. Near the surface, the pattern of vertical displacement resembles the surface topography, (5.4.15), as required by the lower boundary condition. Slightly aloft from the surface at $\tilde{z} = \pi/4$ (Fig. 5.17a), a region of downward displacement forms a U-shaped disturbance over the lee slopes of the mountain and extends some distance downstream. At a level further aloft, such as $\tilde{z} = \pi$ (Fig. 5.17b), the region of downward displacement widens, moves upstream, and is replaced by a U-shaped pattern of upward displacement. The general upstream shift of downward and upward displacement is caused by the upstream phase tilt of upward propagating hydrostatic waves. At greater heights, the zone of disturbance continues to broaden, the disturbance directly in the lee of the mountain disappears, the patterns of upward and downward displacement become more wavelike, due to wave dispersion.

The U-shaped patterns of vertical displacements are explained by a group velocity argument (Smith 1980). The dispersion relation for internal gravity waves in a stagnant Boussinesq fluid may be reduced from (3.6.10)

$$\omega = \frac{\pm NK}{\sqrt{k^2 + l^2 + m^2}}. \quad (5.4.19)$$

With the hydrostatic approximation the above equation becomes

$$\omega = \pm \frac{NK}{m}. \quad (5.4.20)$$

As discussed in Chapter 4, the energy propagation can be described by the group velocity components, which are

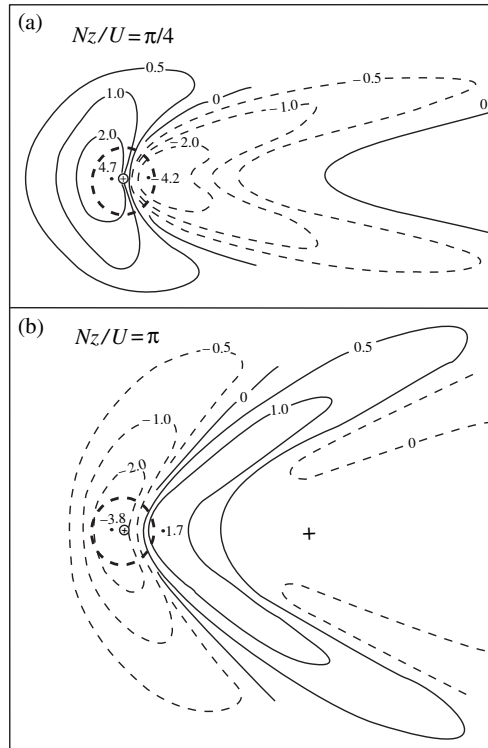


Fig. 5.17 Three-dimensional, linear, hydrostatic stratified flow over a bell-shaped mountain (5.4.15) with $F = U/Nh = 100$. Displayed are the nondimensional vertical displacements at $\tilde{z} = Nz/U =$: (a) $\pi/4$ and (b) π . U-shaped disturbances are associated with the upward propagating wave energy. Solid and dashed curves represent positive and negative values of vertical displacement. The cross marks the position of the mountain peak. The bold, dashed circle is the topographic contour at $r = a$, where r is the distance (radius) from the center of the mountain. These wave patterns are computed by evaluating (5.4.18) numerically using a two-dimensional FFT. (Adapted after Smith 1980.)

$$c_{gx} = \frac{\partial\omega}{\partial k} = \pm \frac{Nk}{mK}; c_{gy} = \frac{\partial\omega}{\partial l} = \pm \frac{Nl}{mK}; c_{gz} = \frac{\partial\omega}{\partial m} = \mp \frac{NK}{m^2} \quad (5.4.21)$$

For steady-state waves on a basic flow, replacing ω by the intrinsic frequency Uk in (5.4.20) leads to

$$m = \frac{\pm NK}{Uk}. \quad (5.4.22)$$

Adding U to c_{gx} , the components of the group velocity in a frame fixed with the Earth become

$$c_{gmx} = \frac{U^2}{K^2}; c_{gmy} = \frac{-Ukl}{K^2}; c_{gmz} = \frac{U^2 k^2}{NK}. \quad (5.4.23)$$

In the coordinates fixed with the mountain or Earth, wave energy propagates from the energy source, i.e. the mountain, along straight lines with slopes

$$\frac{x}{z} = \frac{c_{gm,x}}{c_{gm,z}}; \frac{y}{z} = \frac{c_{gm,y}}{c_{gm,z}}; \frac{y}{x} = \frac{c_{gm,y}}{c_{gm,x}}. \quad (5.4.24)$$

The slope on the horizontal plane y/x may be evaluated from (5.4.23) and (5.4.24),

$$\frac{y}{x} = -\frac{k}{l}, \quad (5.4.25)$$

which is the geometric condition that the phase lines passing through the point (x,y) are radial lines from the origin. Using (5.4.23)–(5.4.24) again gives

$$y^2 = \frac{Nxz}{UK}. \quad (5.4.26)$$

Since the mountain is the source of forcing, the horizontal wavenumber may be approximated by the mountain scale, i.e. $K \approx 1/a$, which yields

$$y^2 = \left(\frac{Nax}{U}\right)z. \quad (5.4.27)$$

Thus, the energy concentrates in a parabola or a U-shaped pattern at a certain height, as shown in Fig. 5.17.

In the above theory, the basic flow speed and Brunt–Vaisala frequency are assumed to be constant with height. In the real atmosphere, they normally vary with height. As in the two-dimensional mountain wave problem, a rapid decrease of the Scorer parameter with height leads to the formation of *trapped lee waves*. The formation of three-dimensional trapped lee waves is similar to that of *Kelvin ship waves* over the water surface. Figure 5.18 shows an example of the cloud streets associated with three-dimensional trapped lee waves produced by airflow past a mountainous island. The wave pattern is generally contained within a wedge with the apex at the mountain. The three-dimensional trapped lee waves are composed by *transverse waves* and *diverging waves*, as depicted in Fig. 5.19. The transverse waves lie approximately perpendicular to the flow direction, and are formed by waves attempting to propagate against the basic flow but that have been advected to the lee. The formation mechanism of transverse waves is the same as that of the two-dimensional trapped lee waves. Unlike the transverse waves, the diverging waves attempt to propagate laterally away from the mountain and have been advected to the lee. Also, the diverging waves have crests that meet the incoming flow at a rather shallow angle. Both of the transverse and diverging waves are mathematically associated with a stationary phase point, and the significant disturbance is confined within a wedge angle of about $19^\circ 28'$ with the x -axis.

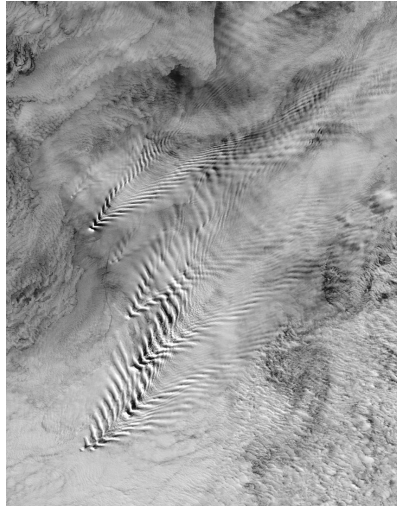


Fig. 5.18 Satellite imagery of three-dimensional trapped lee waves induced by the South Sandwich Islands in the southern Atlantic Ocean on September 18, 2003. The wave pattern is similar to that of the ship waves sketched in Fig. 5.19. (From Visible Earth, NASA.)

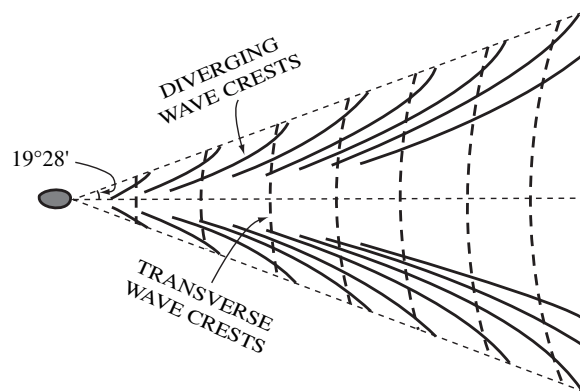


Fig. 5.19 Schematic of transverse (bold-dashed) and diverging (solid) phase lines for a deep water ship wave. (Adapted after Sharman and Wurtele 1983.)

5.4.2 *Generation of lee vortices*

The above linear theory of three-dimensional, stratified flow over mountains provides an in-depth understanding of the dynamics, but it is valid only for high Froude number flow due to the limitations of the small-amplitude (linear) assumption. When the Froude number decreases, the perturbations generated by the mountain become larger and the flow becomes more nonlinear. Due to mathematical intractability, many observed phenomena associated with nonlinear flow over mountains,

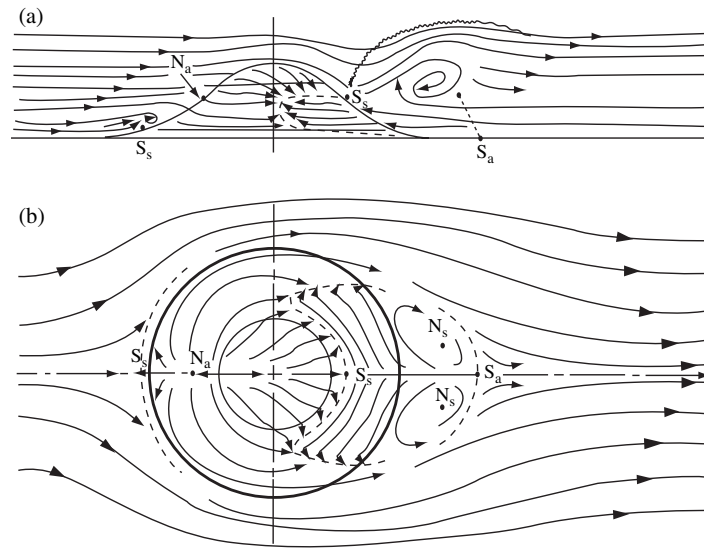


Fig. 5.20 (a) Side view of the mean surface shear stress pattern and streamlines on the center plane of symmetry for a three-dimensional, stratified, viscous flow with $F = U/Nh = 0.4$ past an obstacle with circular contours (e.g., bold solid curve in (b)). In the figure, N and S denote nodes and saddle points, respectively, and subscripts a and s denote attachment and separation, respectively. (b) As (a) but for a plane view of the pattern of surface stress. (Adapted after Hunt and Snyder 1980.)

such as flow recirculation, stagnation points, flow splitting, and lee vortices, have been carried out in tank experiments and by nonlinear numerical simulations.

a. Boundary layer separation

The flow pattern produced by laboratory tank experiments for three-dimensional, stratified flow with relatively large Froude numbers (e.g., $F > 2$) past a bell-shaped mountain is similar to that predicted by linear theory as described in Subsection 5.4.1. Flow patterns are dramatically different for flow with smaller Froude numbers. Figure 5.20 shows a stratified flow with $F = 0.4$ past an isolated mountain in a tank experiment. The most eye-catching phenomenon is a pair of counter-rotating vortices formed in the lee of the obstacle. The formation of this pair of lee vortices is attributed to the *boundary layer separation* mechanism (Batchelor 1967; Hunt and Snyder 1980), as briefly summarized in the following. When the Reynolds number (R_e) is sufficiently high (where $R_e = UL/\nu$, U is the velocity scale, L length scale and ν kinematic viscosity), the boundary-layer flow develops a region of flow reversal near the surface due to an opposing pressure gradient in the direction of flow. The reversed flow meets the incoming flow and forms a stagnation point at which the streamline breaks away from the surface of the obstacle. This process is known as *boundary layer separation*. Mathematically, the streamline of boundary layer separation is a line whose points are singular points of the solutions of the equations of motion in the boundary layer.

For three-dimensional, nonlinear, stratified viscous flow past a symmetric mountain, boundary layer separation first occurs on the center vertical plane before the mountain peak is reached. During the process, several singular points can form. Over the upslope on the center plane, an *attachment point (node of attachment)* N_a forms, which forces part of the flow to recirculate back upstream along the upslope, where it meets the incoming flow, and forms another stagnation point (*saddle point of separation*) S_s (Fig. 5.20a). Downstream of the obstacle on the center vertical plane, flow separates and forms a third stagnation point(s) (*saddle points of attachment*) S_a . The separated flow recirculates on this vertical plane, meets with the downslope flow and forms another saddle point of separation (S_s) over the lee slope. On the surface (Fig. 5.20b), the recirculated flow from N_a forces the incoming flow to split (i.e. *flow splitting*) at S_s and part of the split flow recirculates and forms a pair of stationary lee vortices centered at the *nodes of separation* (N_s). If the Froude number is decreased further, this flow pattern persists, but N_a moves closer to the mountain peak and the lee vortices expand further downstream. Although an unrealistically large mountain slope of $O(1)$, compared to that in the real world is often used in laboratory experiments, the simulated flow features are very similar to those observed in the real atmosphere.

b. Generation of lee vortices in an inviscid fluid

Using a nonlinear numerical model with free-slip lower boundary condition, a pair of counter-rotating vortices was found to form on the lee of an isolated mountain when a low-Froude number (e.g., $F = 0.66$, Fig. 5.21a), three-dimensional, stratified, uniform flow passes over the mountain (Smolarkiewicz and Rotunno 1989). The simulated results agree fairly well with laboratory tank experiments as shown in Fig. 5.20. The free-slip lower boundary condition implies no explicit surface friction is included in the model atmosphere. Although linear theory breaks down, at least locally, the vertical displacement field (Fig. 5.21c) still resembles the U-shaped pattern found in the linear theory described in Subsection 5.4.1 (Fig. 5.17). A large-amplitude mountain wave develops over the mountain peak (Fig. 5.21e). The trough of the vertically propagating gravity waves in Fig. 5.21e shifts upstream and becomes narrower, indicating a tendency toward collapse of the isentropic surfaces on the lee slopes of the mountain, which is also in agreement with the linear theory. Since the air parcels are able to flow almost directly across the mountain, this flow regime is characterized as the *flow-over regime*.

When the Froude number is reduced to approximately below 0.5, such as $F = 0.22$ (Fig. 5.21b), a pair of counter-rotating vortices forms on the lee side and a saddle point of separation and a node of attachment are produced on the upstream side of the mountain, strikingly similar to the results obtained in laboratory experiments (Fig. 5.20b). The region of downward displacement is enlarged (Fig. 5.21d). The gravity wave response is drastically reduced, as much of the airflow is diverted around the flanks of the mountain and the disturbance appears to be much more horizontal (Fig. 5.21f). Below the mountain top, there is a recirculating flow associated with the

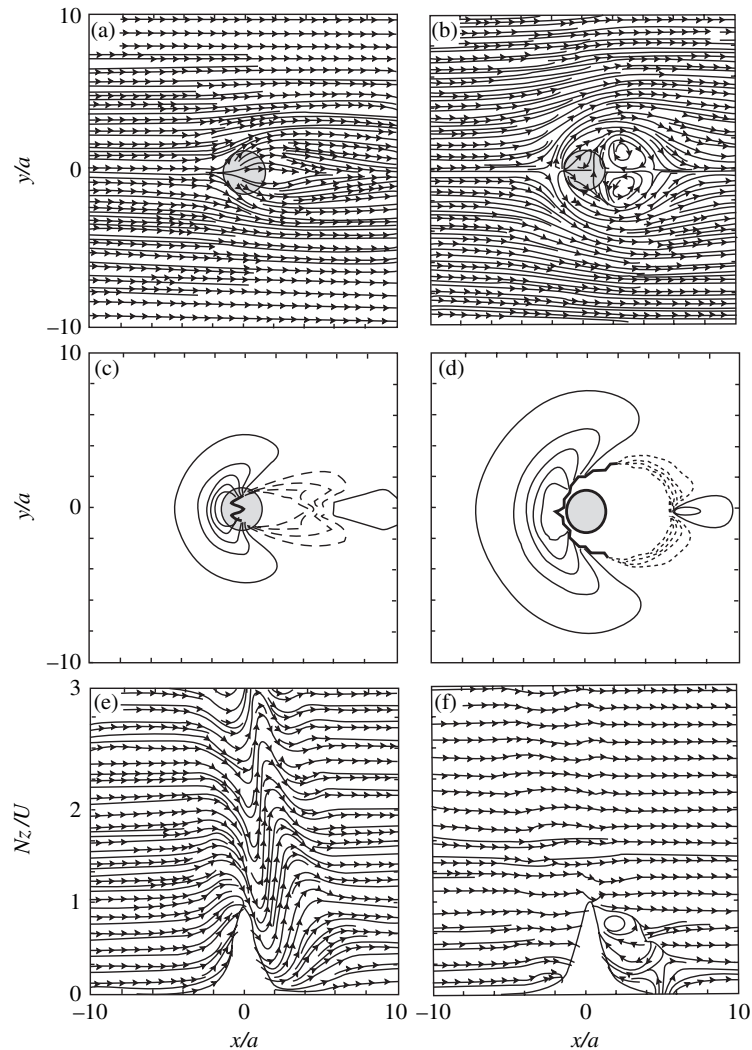


Fig. 5.21 Three-dimensional, stratified, uniform flow with no surface friction over a bell-shaped mountain simulated by a nonlinear numerical model. Surface streamlines, vertical displacements at $Nz/U = \pi/4$, and streamlines in the vertical plane $y/a = 0$ after $Ut/a = 9$ are shown in (a), (c), and (e), respectively, for the case with $F = 0.66$. The same flow fields but for $F = 0.22$ are shown in the right panels ((b), (d) and (f)). The simulated flow fields have reached quasi-steady state. The flow and orographic parameters are: $U = 10 \text{ m s}^{-1}$ or 3.3 m s^{-1} , $N = 0.01 \text{ s}^{-1}$, $h = 1.5 \text{ km}$, and $a = 10 \text{ km}$, which give $F = 0.66$ or 0.22 , respectively. The bell-shaped mountain is prescribed by (5.4.15.). (Adapted after Smolarkiewicz and Rotunno 1989.)

lee vortices. This flow regime is characterized as the *flow-around regime*. Based on the nondimensional mountain height (or inverse Froude number – Nh/U) and horizontal mountain aspect ratio (b/a), four classes of wave and flow phenomena of importance in three-dimensional, stratified, uniform, hydrostatic flow past an isolated mountain

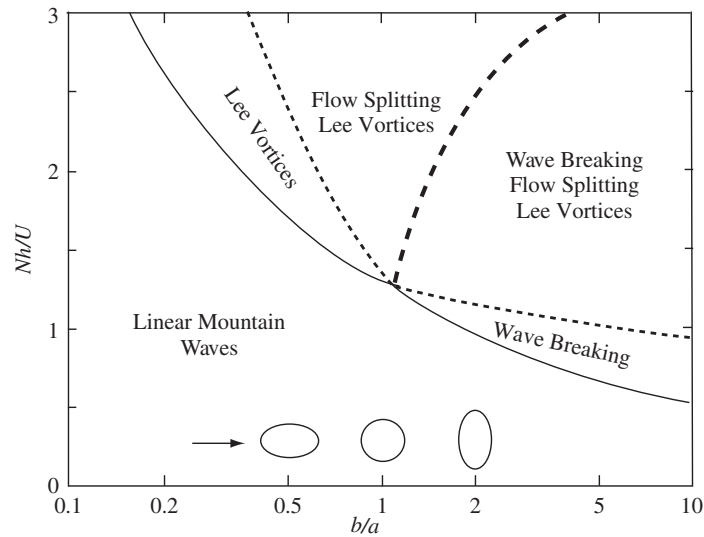


Fig. 5.22 Regime diagram for three-dimensional, stratified, uniform, hydrostatic flow over an isolated mountain. The flow regime is controlled by the horizontal mountain aspect ratio (b/a) and the nondimensional height or the inverse Froude number (Nh/U), where a and b are the mountain scales in along (x) and perpendicular (y) to the basic flow directions, respectively. Four classes of phenomena of importance in this type of flow are: (1) linear mountain waves, (2) wave breaking, (3) flow splitting, and (4) lee vortices. The circles/ellipses represent the mountain contours. (Adapted after Smith 1989a and Epifanio 2003.)

can be identified (Fig. 5.22): (1) linear mountain waves, (2) wave breaking, (3) flow splitting, and (4) lee vortices.

The key question concerning the numerically simulated lee vortices as shown in Fig. 5.21 is the source of vorticity. In the absence of surface friction, boundary layer separation will not occur and thus cannot be held responsible for the formation of the lee vortices. Although many detailed dynamics of this problem are still topics of current research, the basic dynamics for the generation of lee vortices can be understood through the following two major theories: (1) *tilting of baroclinically generated vorticity* (Smolarkiewicz and Rotunno 1989) and (2) *generation of internal potential vorticity* by turbulence dissipation in numerical simulations (Smith 1989b; Schär and Smith 1993a, b).

c. Tilting of baroclinically generated vorticity

The mechanism of baroclinically generated vorticity tilting can be understood by taking cross differentiations of (2.2.1)–(2.2.3) to yield the inviscid vorticity equation

$$\frac{\partial \boldsymbol{\omega}}{\partial t} = -\mathbf{V} \cdot \nabla \boldsymbol{\omega} + (\boldsymbol{\omega} \cdot \nabla) \mathbf{V} + \frac{\nabla \rho \times \nabla p}{\rho^2}, \quad (5.4.28)$$

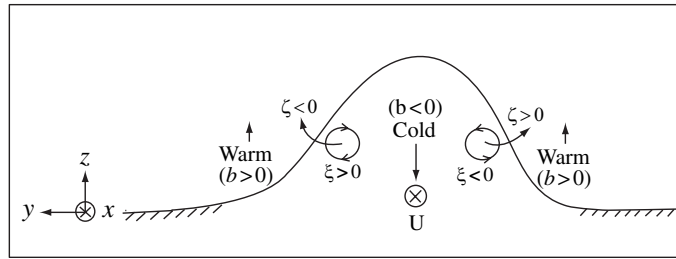


Fig. 5.23 A schematic diagram showing the generation of leeside vorticity by the vertical tilting of baroclinically generated horizontal vorticity (Smolarkiewicz and Rotunno 1989). The downward (upward) arrow below the adiabatically-induced cold (warm) region denotes downward (upward) motion. A negative x -vorticity, $\xi < 0$, is produced over the right-hand side of the upslope baroclinically by the relatively cold air ($b < 0$) along the center line and the relatively warm air to the right (facing downstream), as indicated by (5.4.29). This negative x -vorticity is then swept downstream and produces a positive vertical vorticity, $\zeta > 0$, on the right-hand side of the lee due to the vertical tilting of the x -vorticity, as implied by (5.4.28).

where $\boldsymbol{\omega} = \nabla \times \boldsymbol{V} = (\xi, \eta, \zeta)$ is the three-dimensional *vorticity vector*. The last term on the right side of the above equation represents the generation of vorticity by baroclinicity. Once local vorticity anomalies are generated, they are advected by the flow field through the first term or tilted and stretched through the second term on the right-hand side of (5.4.28). For mountains with small aspect ratio of the obstacle height and horizontal width, the baroclinicity term reduces to (e.g., Epifanio 2003):

$$\frac{\nabla \rho \times \nabla p}{\rho^2} \approx -\mathbf{k} \times \nabla b, \quad (5.4.29)$$

where b is the buoyancy.

Figure 5.23 shows a schematic diagram depicting the generation of leeside vorticity by the vertical tilting of baroclinically generated horizontal vorticity. A negative x -vorticity, $\xi < 0$, is generated on the right upslope baroclinically by the relatively cold air along the center line and the relatively warm air to the right (facing downstream), as indicated by (5.4.29). This negative x -vorticity is then swept downstream and produces a positive vertical vorticity, $\zeta > 0$, to the lee by the vertical tilting of the x -vorticity, as implied by (5.4.28). Similarly, a positive x -vorticity anomaly generated over the left upslope is tilted into a negative vertical vorticity to the lee. As these vertical vorticity anomalies intensify, recirculating warm-core eddies develop as a result of reconnection. This mechanism dominates during the rapid start-up, early stage, over a nondimensional time $Ut/a = O(1)$, in which the flow is essentially inviscid and adiabatic and the potential vorticity (PV) is conserved (Schär and Durran 1997).

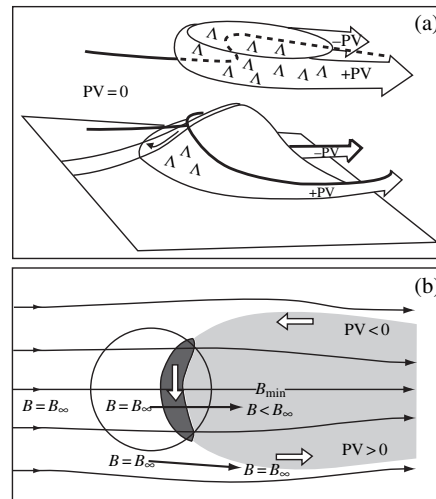


Fig. 5.24 (a) A conceptual model depicting potential vorticity (PV) generation by turbulence dissipation at stagnation points associated with wave breaking aloft and upstream blocking. The symbol “^^^” denotes areas of turbulence generated by wave breaking or blocking. (Adapted after Smith 1989a.) (b) Schematic depiction of the relationship between PV generation and Bernoulli function on an isentropic surface in steady-state, stratified flow over the wave breaking region. Thin lines are streamlines and dark-shaded area over the lee slope denotes a localized region of dissipation due to wave breaking, a hydraulic jump or blocking. The gray shaded area extending downstream denotes a reduced Bernoulli function. Open arrows denote the PV flux \mathbf{J} associated with the Bernoulli gradient on the isentropic surface as described by (5.4.35). (From Schär and Durran 1997.)

d. Generation of potential vorticity by turbulence dissipation

At a later stage, the associated thermal anomalies generated by baroclinicity are eroded by dissipative and diffusive processes, whereby the warm surface anomalies are converted into PV. During this stage, the flow is controlled by dissipation and is accompanied by the PV generation over a nondimensional time of $O(10)$ – $O(100)$ (Schär and Durran 1997). Note that the *conservation of potential vorticity* is violated in regions of *flow stagnation*, such as in the region of upstream blocking where the isentropic surface intersects the ground, and the region of wave breaking above the lee slope where turbulence occurs (Fig. 5.24a). The dynamics of dissipative generation of PV is directly linked to the reduction in the Bernoulli function within the wake, as demonstrated in steady shallow-water flow past an obstacle (Schär and Smith 1993a). The shallow-water theory can be extended to stratified fluid flow by considering the PV (q) which satisfies a conservative equation of the form (Haynes and McIntyre 1990):

$$\frac{\partial(\rho q)}{\partial t} + \nabla \cdot \mathbf{J} = 0, \quad (5.4.30)$$

where q is defined as

$$q = \frac{\nabla\theta \cdot \boldsymbol{\omega}_a}{\rho}, \quad (5.4.31)$$

and the total PV flux (\mathbf{J}) is given by

$$\mathbf{J} = \rho q \mathbf{V} - (\dot{Q} \boldsymbol{\omega}_a + \mathbf{F} \times \nabla\theta). \quad (5.4.32)$$

In the above equation, \dot{Q} ($\equiv D\theta/Dt$) is the diabatic heating, $\boldsymbol{\omega}_a$ the three-dimensional absolute vorticity vector, and \mathbf{F} the viscous force per unit mass. In this section, we have assumed that the Earth rotation is negligible thus $\boldsymbol{\omega}_a = \boldsymbol{\omega}$.

It can be shown that

$$\mathbf{J} = \nabla\theta \times \left(\nabla B + \frac{\partial \mathbf{V}}{\partial t} \right) - \boldsymbol{\omega} \frac{\partial \theta}{\partial t}, \quad (5.4.33)$$

where

$$B = \mathbf{V} \cdot \mathbf{V} / 2 + c_p T + gz \quad (5.4.34)$$

is the *Bernoulli function*. In a steady-state flow, the Bernoulli function is conserved following the flow. In addition, (5.4.33) reduces to

$$\mathbf{J} = \nabla\theta \times \nabla B = \frac{\partial \theta}{\partial \mathbf{n}} \mathbf{n} \times \nabla B, \quad (5.4.35)$$

where \mathbf{n} is a unit vector oriented perpendicular to the isentropic surface and pointing toward warm air. The *generalized Bernoulli's theorem* (Schär 1993), (5.4.35), indicates that non-zero PV fluxes must be present where there is a variation in the Bernoulli function along any isentropic surface. Figure 5.24b shows a schematic of PV generation by turbulence dissipation on an isentropic surface in steady-state stratified flow past an isolated mountain. The narrow dissipative region may be produced by turbulence associated with wave breaking, a hydraulic jump or blocking, and generates Bernoulli function deficit in the wake extending downstream. Based on Fig. 5.24 and (5.4.34), PV is generated in the dissipative region and advected downstream along the edge of the wake. A pair of counter-rotating vortices may form in the wake if the vertical vorticity associated with the generated PV is sufficiently strong.

It appears that the above PV analysis is able to explain the close relationship between dissipative turbulence and PV generation for a low-Froude number, stratified flow over an isolated mountain. The causality, however, is still unclear due to the steady-state assumption. In addition, an assumption of balance is required in order to infer the structure of the flow from the distribution of PV (Hoskins *et al.* 1985). In the near field of the wake, these balance constraints are constantly strongly violated due to the presence of the strong surface temperature gradient over the lee slope, which results from the upstream blocking (Epifanio and Rotunno 2005). Therefore, although the PV generation

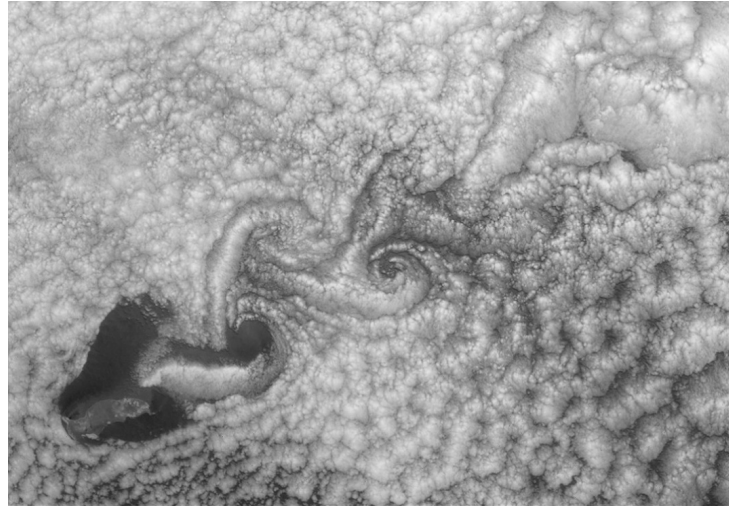


Fig. 5.25 A von Kármán vortex street that formed to the lee of the Guadalupe Island, off the coast of Mexico's Baja Peninsula, revealed by MISR images from June 11, 2000 detected by NASA satellite Terra. (From Visible Earth, NASA.)

may have important implications on the downstream evolution of orographic wakes and lee vortices, a fundamental understanding of the wake formation is still needed.

When the wake flow in which the lee vortices are embedded becomes unstable, the vortices tend to shed downstream and form a *von Kármán vortex street*. A von Kármán vortex street is a repeating pattern of alternate and swirling vortices along the center line of the wake flow, and is named after the fluid dynamicist, Theodore von Kármán. This process is also known as *vortex shedding*. Any noise, impulsive disturbance, or asymmetric forcing in the wake flow can trigger an instability, which gives way to a vortex street or vortex shedding. Figure 5.25 shows an example of a von Kármán vortex street formed in the atmosphere to the lee of a mountainous island. The von Kármán vortex street or vortex shedding has also been simulated by many nonlinear numerical models, such as that shown in Fig. 5.28a.

5.5 Flows over larger mesoscale mountains

5.5.1 Rotational effects

In the previous sections, effects of Earth's rotation are neglected. This is approximately valid for flow with Rossby number ($R_o = U/fL$, where L is the horizontal scale of the mountain) much larger than 1. However, for flow over mountains with $R_o = O(1)$ or smaller, the effects of Earth's rotation cannot be ignored. In this situation, the advection time for an air parcel to pass over the mountain is too large to be ignored compared to the period of inertial oscillation due to Earth's rotation ($2\pi/f$). Flow past many mesoscale mountain ranges, such as the European Alps, US Rockies, Canadian Rockies, Andes, the